

¹ **Differential response of a tree-killing bark beetle to forest structure
2 and composition across a gradient of climatic water deficit**

³ Michael J. Koontz^{1,2,3*}, Andrew M. Latimer^{1,2}, Leif A. Mortenson⁴, Christopher J. Fettig⁵, Malcolm P.
⁴ North^{1,2,6}

⁵ ¹Graduate Group in Ecology, University of California, Davis, CA, USA

⁶ ²Department of Plant Sciences, University of California, Davis, CA, USA

⁷ ³Earth Lab, University of Colorado-Boulder; Boulder, CO, USA

⁸ ⁴USDA Forest Service, Pacific Southwest Research Station, Placerville, CA, USA

⁹ ⁵USDA Forest Service, Pacific Southwest Research Station, Davis, CA, USA

¹⁰ ⁶USDA Forest Service, Pacific Southwest Research Station, Mammoth Lakes, CA, USA

¹¹ *Correspondence: michael.koontz@colorado.edu

¹² *Keywords:* bark beetles, forest structure, drones, climatic water deficit, Sierra Nevada, California, disturbance,
¹³ structure from motion, *Dendroctonus brevicomis*, *Pinus ponderosa*, threshold dynamics

¹⁴ *Abstract word count:* 427

¹⁵ *Main text word count:* 6582 (Intro: 1162; Methods: 3277 (519+420+115+331+332+278+468+504+310);

¹⁶ Results: 246 (41+205); Discussion: 1897

¹⁷ *Text boxes word count:* 0

¹⁸ Date report generated: September 15, 2019

¹⁹ **Abstract**

²⁰ The Californian hot drought of 2012 to 2015 created favorable conditions for unprecedented ponderosa pine
²¹ (*Pinus ponderosa*) mortality in the Sierra Nevada mountain range, largely caused by the western pine beetle
²² (*Dendroctonus brevicomis*). Climate conditions related to tree water stress as well as forest structure and
²³ composition can influence the severity of forest insect disturbance, but it remains challenging to consider how
²⁴ these variables may interact to produce patterns of tree mortality. Previous studies have shown an interaction
²⁵ between climate conditions and forest density in their effect on tree mortality, but density is a coarse gauge
²⁶ of forest structure that can affect western pine beetle behavior in a number of ways. Measuring broad-scale
²⁷ climate conditions simultaneously with complex forest structure— including tree species, tree size, and local
²⁸ density— will refine our understanding of how these variables interact, but is generally expensive and/or
²⁹ labor-intensive. We overcame these hurdles using aerial drone surveys over an established network of 160

30 forest plots along a 350km and 1000m elevation gradient in western slope Sierra ponderosa pine/mixed-conifer
31 forests. Using Structure from Motion (SfM) processing on over 450,000 images and field measurements from
32 the coincident ground plots, we determined tree size, location, and species for individual trees over 9km² of
33 forest that experienced ponderosa pine mortality as a result of western pine beetle colonization. We modeled
34 the probability of ponderosa pine mortality as a linear combination of forest structure variables and site-level
35 climatic water deficit, and used a Gaussian process to estimate the spatial covariance in the response.

36 We found that greater host density strongly increased the probability of host mortality, and greater host
37 size generally decreased the probability of host mortality. There was also a strong three-way interaction
38 between host density, host size, and climatic water deficit such that host density and host size tended to
39 synergistically increase the probability of host mortality at hot/dry sites, but denser, smaller trees tended to
40 drive mortality in cool/wet sites.

41 Our results demonstrate a variable response of the western pine beetle to complex forest structure and
42 composition across an environmental gradient during the same hot drought, which may indicate forest sites
43 were in different stages of disturbance (from “endemic” to “outbreak”) depending on their regional climate.
44 Management interventions that reduce host density may decrease the probability of tree mortality attributed
45 to western pine beetles in the future, and our results suggest that focusing these treatments on areas that are
46 most likely to exceed feedback thresholds (i.e., hot/dry sites with many available hosts) will have the best
47 chance of increasing tree survivorship, specifically of larger trees.

48 Introduction

49 Bark beetles dealt the final blow to many of the nearly 150 million trees killed in the California hot drought
50 of 2012 to 2015 and its aftermath (USDAFS 2019). A harbinger of climate change effects to come, record
51 high temperatures exacerbated the drought (Griffin and Anchukaitis 2014), which increased water stress on
52 trees (Asner et al. 2016), making them more susceptible to colonization by bark beetles (Fettig 2012, Kolb et
53 al. 2016). Further, a century of fire suppression policy has enabled forests to grow into dense stands, which
54 also makes them more vulnerable to bark beetles (Fettig 2012). This combination of environmental conditions
55 and forest structural characteristics led to tree mortality events of unprecedented size in the driest, densest
56 forests across the state (Young et al. 2017). The mechanisms underlying the link between tree susceptibility
57 to colonization by insects and hot, dry conditions are often directly attributed to tree physiology (Bentz et al.
58 2010), while the link to forest density is multifaceted (Fettig 2012). Because forest density is a coarse metric
59 of the forest features to which bark beetles respond (Raffa et al. 2008), our understanding of the connection
60 between forest density and insect disturbance severity could be enhanced with more finely-resolved measures

61 of forest structure as well as explicit consideration of species composition (Stephenson et al. 2019, Fettig et al.
62 2019). Finally, the challenge of simultaneously measuring the effects of both local-scale forest features (such
63 as structure and composition) and broad-scale environmental conditions on forest insect disturbance leaves
64 their interaction effect relatively underexplored (Seidl et al. 2016, Stephenson et al. 2019, Fettig et al. 2019).

65 The ponderosa pine/mixed-conifer forests in California's Sierra Nevada region are characterized by regular
66 bark beetle disturbances, primarily by the influence of western pine beetle (*Dendroctonus brevicomis*; WPB)
67 on its host ponderosa pine (*Pinus ponderosa*) (Fettig 2016). The WPB is a "primary" bark beetle— its
68 reproductive success is contingent upon host tree mortality, which itself requires enough beetles to "mass
69 attack" the host tree and overwhelm its defenses (Raffa and Berryman 1983). This Allee effect creates a
70 strong coupling between beetle selection behavior of host trees and host tree susceptibility to colonization
71 (Raffa and Berryman 1983, Logan et al. 1998). A key defense mechanism of trees to bark beetle attack is to
72 flood beetle bore holes with resin, which physically expels beetles and may interrupt beetle communication
73 (Franceschi et al. 2005, Raffa et al. 2015). Under normal conditions, weakened trees with compromised
74 defenses are the most susceptible to colonization and will be the main targets of primary bark beetles like
75 the western pine beetle (Bentz et al. 2010, Raffa et al. 2015). Under severe water stress, many trees no
76 longer have the resources available to mount a defense (Kolb et al. 2016) and thus prolonged drought can
77 often trigger increased bark beetle-induced tree mortality as average tree vigor declines (Bentz et al. 2010).
78 As local population density of beetles increases due to successful reproduction within spatially-aggregated
79 weakened trees, as might occur during drought, mass attacks grow in size and become capable of overwhelming
80 formidable tree defenses such that even healthy trees may be susceptible to colonization and mortality (Bentz
81 et al. 2010, Raffa et al. 2015). Thus, water stress can be a key determinant of whether individual trees are
82 susceptible to bark beetles under many conditions, and this environmental condition may interact with beetle
83 population dynamics to drive tree susceptibility under extreme conditions (Bentz et al. 2010, Stephenson et
84 al. 2019).

85 Western pine beetle activity is strongly influenced by forest structure—the spatial distribution and size of
86 trees—and tree species composition. Considering forest structure alone, high-density forests are more prone to
87 bark beetle-induced tree mortality (Fettig 2012) which may arise as greater competition for water resources
88 amongst crowded trees and thus average tree resistance is lower (Hayes et al. 2009), or because smaller gaps
89 between trees protect pheromone plumes from dissipation by the wind and thus enhance intraspecific beetle
90 communication (Thistle et al. 2004). Tree size is another aspect of forest structure that affects bark beetle
91 host selection behavior with smaller trees tending to have lower capacity for resisting attack, and larger
92 trees being a more desirable target on account of their thicker phloem providing greater nutritional content

93 (Chubaty et al. 2009, Graf et al. 2012). Considering forest composition alone, WPB activity in the Sierra
94 Nevada range of California is necessarily tied to the regional distribution of its exclusive host, ponderosa
95 pine (Fettig 2016). Colonization by primary bark beetles can also depend on the relative frequencies of tree
96 species in a more local area, akin to reduced oligophagous insect herbivory in forests comprising taxonomically
97 distinct tree species compared to monocultures (Jactel and Brockerhoff 2007). The interaction between
98 forest structure and composition also drives WPB activity. For instance, high density forests with high host
99 availability may experience greater beetle-induced tree mortality because dispersal distances between potential
100 host trees are shorter and facilitate successful colonization (Miller and Keen 1960, Berryman 1982, Fettig et al.
101 2007) or because high host availability reduces the chance of individual beetles wasting their limited resources
102 flying to and landing on a non-host tree (Moeck et al. 1981, Evenden et al. 2014). Stand-scale measures of
103 forest structure and composition thus paint a fundamentally limited picture of the mechanisms by which
104 these forest characteristics affect bark beetle disturbance, but finer-grain information explicitly recognizing
105 tree size, species, and local tree density should more appropriately capture the ecological processes underlying
106 insect-induced tree mortality. Additionally, considering the effects of local forest structure and composition
107 with the effects of environmental conditions may help refine our understanding of tree mortality patterns in
108 widespread events such as during the recent California hot drought.

109 The vast spatial extent of tree mortality in the 2012 to 2015 California hot drought challenges our ability to
110 simultaneously consider how broad-scale environmental conditions may interact with local forest structure
111 and composition to affect the dynamic between bark beetle selection and colonization of host trees, and host
112 tree susceptibility to attack (Anderegg et al. 2015, Stephenson et al. 2019). Measuring local forest structure
113 generally requires expensive instrumentation (Kane et al. 2014, Asner et al. 2016) or labor-intensive field
114 surveys (Larson and Churchill 2012, Stephenson et al. 2019, Fettig et al. 2019), which constrains survey
115 extent and frequency. Small, unhumanned aerial systems (sUAS) enable relatively fast and cheap remote
116 imaging over dozens of hectares of forest, which can be used to measure complex forest structure at the
117 individual tree scale (Morris et al. 2017, Shiklomanov et al. 2019). Distributing such surveys across an
118 environmental gradient can overcome the data acquisition challenge inherent in investigating phenomena
119 with both a strong local- and a strong broad-scale component.

120 We used ultra-high resolution, sUAS-derived remote sensing data over a network of 32 sites in Sierra Nevada
121 ponderosa pine/mixed-conifer forests spanning 1000m of elevation and 350km of latitude (see Fettig et al.
122 (2019)) and covering a total of 9km² to ask how broad-scale environmental conditions interacted with local,
123 complex forest structure to affect the probability of tree mortality during the cumulative tree mortality event
124 of 2012 to 2018. We asked:

- 125 1. How does host tree density and average host tree size affect WPB-induced tree mortality?
- 126 2. How does the density of all tree species (hereafter “overall density”) and average tree size of all species
- 127 (hereafter “overall size”) affect WPB-induced tree mortality?
- 128 3. How does environmentally-driven tree moisture stress affect WPB-induced tree mortality?
- 129 4. Do the effects of forest structure, forest composition, and environmental condition interact to influence
- 130 WPB-induced tree mortality?

131 **Methods**

132 **Study system**

133 The study sites were chosen to reflect typical west-side Sierra Nevada yellow pine/mixed-conifer forests and

134 were dominated by ponderosa pine trees, *Pinus ponderosa* (Fettig et al. 2019), whose primary bark beetle

135 predator in California is the western pine beetle (WPB), *Dendroctonus brevicomis*. The typical life cycle

136 of WPBs consists of pioneer beetles dispersing to a new host tree, determining the host’s susceptibility to

137 attack, and using pheromone signals to attract other WPBs. The attracted WPBs mass attack the tree by

138 boring into its inner bark, laying eggs, and dying, leaving their offspring to develop inside the doomed tree

139 before themselves dispersing to a new potential host (Raffa et al. 2008). In California, the WPB can have 2-3

140 generations in a single year and can often out-compete its congener, the mountain pine beetle, *Dendroctonus*

141 *ponderosa* (MPB), for the ponderosa pine host (Fettig et al. 2019).

142 We built our study on 180 vegetation/forest insect monitoring plots at 36 sites established between 2016

143 and 2017 by Fettig et al. (2019) (Figure 1). These established plots were located in WPB-attacked, yellow

144 pine/mixed-conifer forests across the Eldorado, Stanislaus, Sierra and Sequoia National Forests and were

145 stratified by elevation (914-1219 meters [3000-4000 feet], 1219-1524 meters [4000-5000 feet], 1524-1828 meters

146 [5000-6000 feet] above sea level). In the Sequoia National Forest, the southernmost National Forest in our

147 study, plots were stratified with the lowest elevation band between 1219 and 1524 meters (4000-5000 feet) and

148 extended to an upper elevation band of 1828-2133 meters (6000-7000 feet) to capture a more similar forest

149 community composition as at the more northern National Forests. The sites have variable forest structure

150 and plot locations were selected in areas with >40% ponderosa pine basal area and >10% ponderosa pine

151 mortality. At each site, five 0.04 ha circular plots were installed along transects with between 80 and 200m

152 between each plot. In the field, Fettig et al. (2019) mapped all stem locations relative to the center of each

153 plot using azimuth/distance measurements. Tree identity to species, tree height, and diameter at breast

154 height (DBH) were recorded if DBH was greater than 6.35cm. Year of mortality was estimated based on

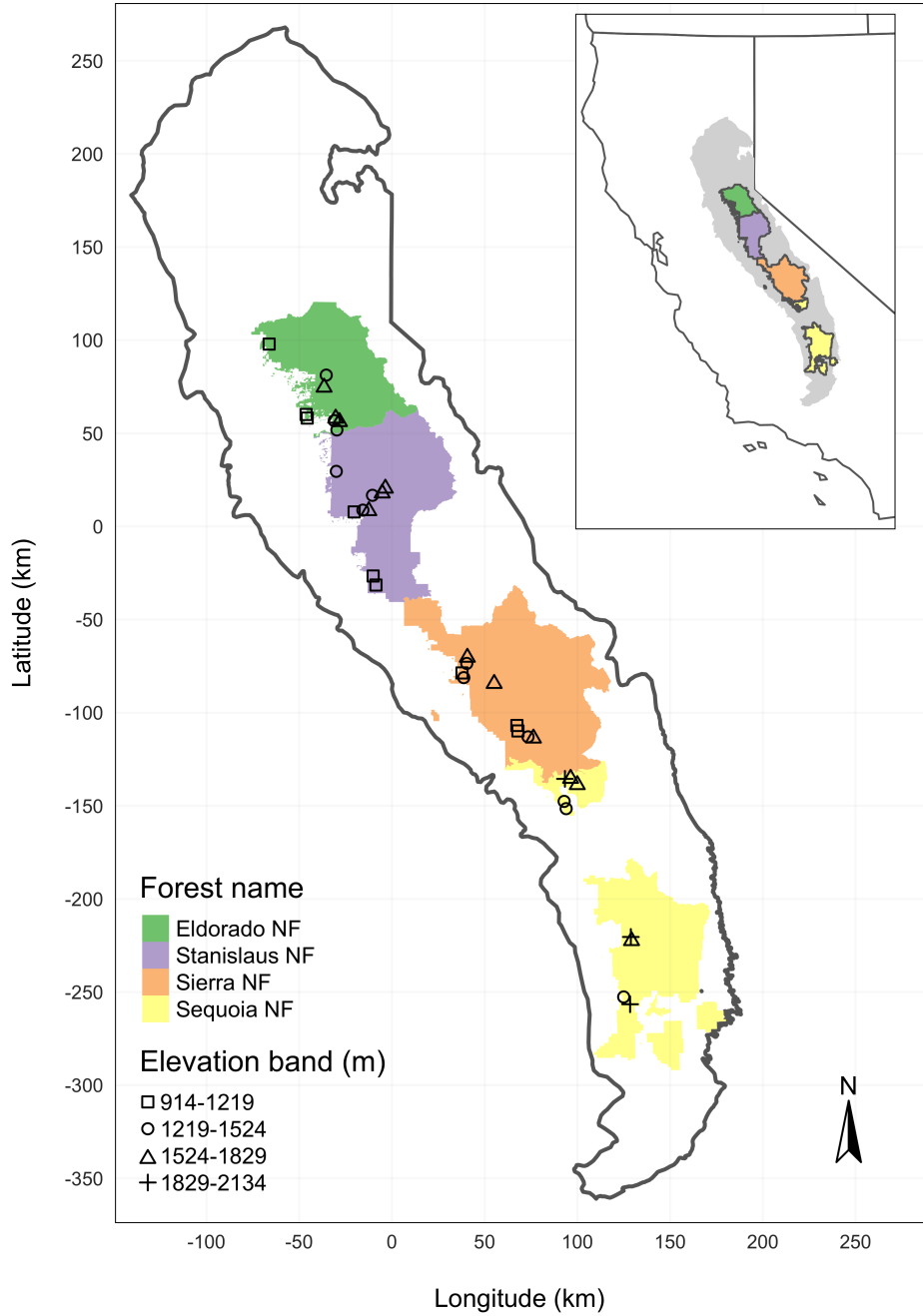


Figure 1: The network of field plots spanned a 350 km latitudinal gradient from the Eldorado National Forest in the north to the Sequoia National Forest in the south. Plots were stratified by three elevation bands in each forest, with the plots in the Sequoia National Forest (the southern-most National Forest) occupying elevation bands 305m above the three bands in the other National Forests in order to capture a similar community composition.

needle color and retention, if it wasn't directly observed between site visits. A small section of bark was removed from dead trees to confirm insect activity. During the spring and early summer of 2018, all field plots were revisited to assess whether dead trees had fallen (Fettig et al. 2019).

Instrumentation

Imagery was captured using a DJI Zenmuse X3 RGB camera (DJI 2015a) and a Micasense RedEdge3 5-band multispectral camera (Micasense 2015). We mounted both of these instruments simultaneously on a DJI Matrice 100 aircraft (DJI 2015b) using the DJI 3-axis stabilized gimbal for the Zenmuse X3 camera and a Micasense angled fixed mount for the RedEdge3 camera. The gimbal and the angled fixed mount ensured both instruments were nadir-facing during image capture. Just prior to or after image capture at each site, we calibrated the RedEdge3 camera by taking an image of a calibration panel on the ground in full sun with known reflectance values for each of the 5 narrow bands (Table 1).

Table 1: Reflectance sensitivity of the Micasense Rededge3 camera. The calibration panel value represents the reflectance of the calibration panel for the given wavelength.

Band number	Band name	Center wavelength	Band width	Wavelength range	Panel reflectance
1	blue (b)	475	20	465-485	0.64
2	green (g)	560	20	550-570	0.64
3	red (r)	668	10	663-673	0.64
4	near infrared (nir)	840	40	820-860	0.6
5	red edge (re)	717	10	712-722	0.63

Flight protocol

Image capture was conducted as close to solar noon as possible to minimize shadow effects (varying primarily due to site accessibility; always within 4 hours, usually within 2 hours). Prior to the aerial survey, two strips of bright orange drop cloth (~100cm x 15cm) were positioned as an "X" over the permanent monuments marking the center of the 5 field plots from Fettig et al. (2019).

For each of the 36 sites (containing 5 plots each), we captured imagery over the surrounding ~40 hectares of forested area using north-south aerial transects. For three sites, we surveyed less surrounding area in order to maintain visual and radio communication with the aircraft during flight which can be obstructed by rolling terrain or non-centrally available takeoff locations.

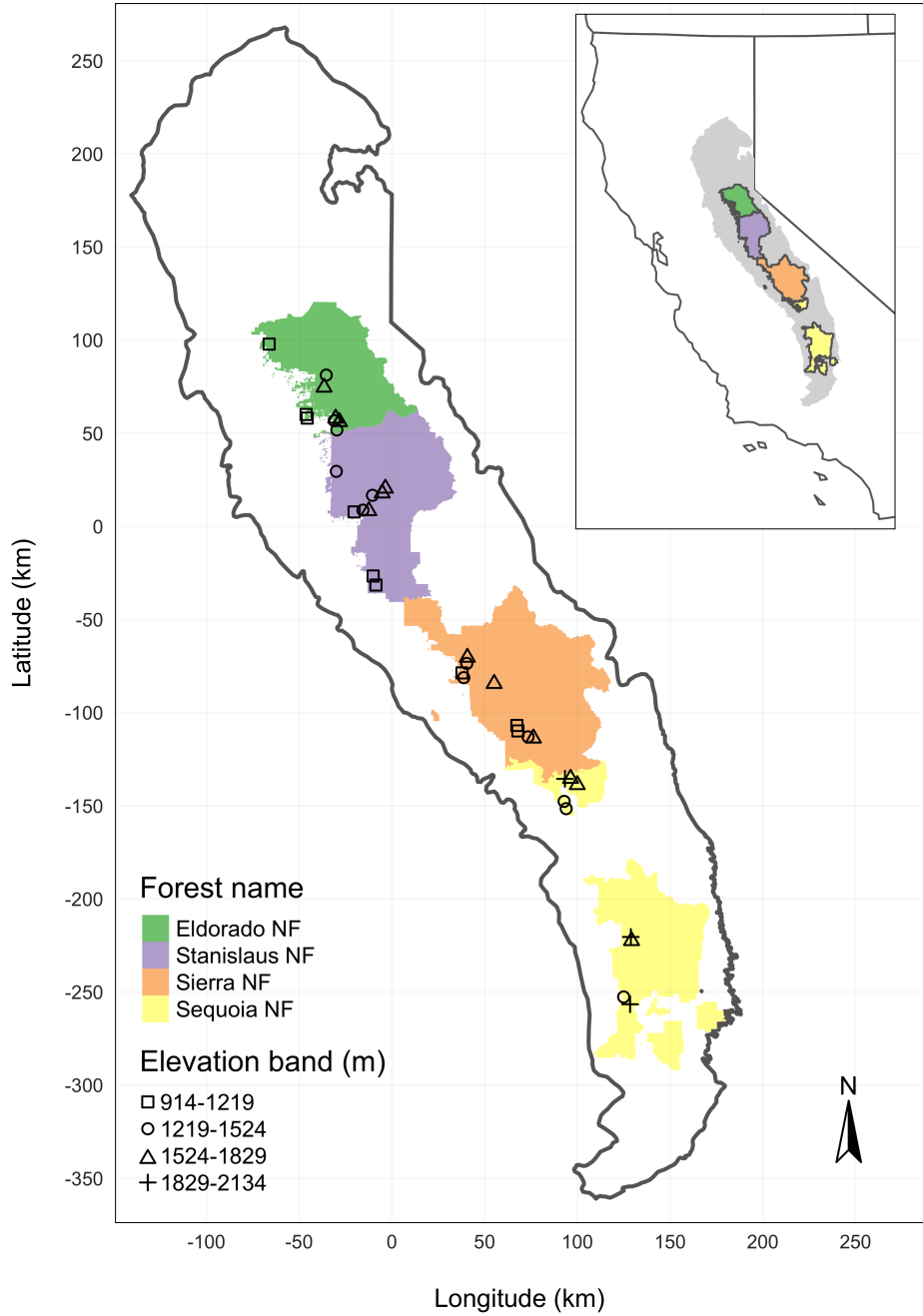


Figure 1: The network of field plots spanned a 350 km latitudinal gradient from the Eldorado National Forest in the north to the Sequoia National Forest in the south. Plots were stratified by three elevation bands in each forest, with the plots in the Sequoia National Forest (the southern-most National Forest) occupying elevation bands 305m above the three bands in the other National Forests in order to capture a similar community composition.

175 We preprogrammed aerial transects using Map Pilot for DJI on iOS flight software (hereafter Map Pilot)
176 (DronesMadeEasy 2018). Using the Map Pilot software, we included an altitude adjustment along each
177 aerial transect using a 1-arc-second digital elevation model (Farr et al. 2007) such that the aircraft's altitude
178 remained approximately constant at 120 meters above ground level in order to maintain consistent ground
179 sampling distance (centimeters on the ground per pixel) in the imagery. Ground sampling distance was
180 approximately 5 cm/px for the Zenmuse X3 RGB camera and approximately 8 cm/px for the RedEdge3
181 multispectral camera. For this analysis, we dropped 4 sites whose imagery was of insufficient quality to
182 process.

183 Structure from motion (SfM) processing requires highly overlapping images, especially in densely vegetated
184 areas (Frey et al. 2018). We planned transects with 90% forward overlap and 90% side overlap at 100 meters
185 below the lens. Thus, with flights being at 120 meters above ground level, we achieved slightly higher than
186 90/90% overlap for objects under 20 meters tall (91.6/91.6% overlap at the ground). Overlap values were
187 based on focal length (3.6mm), sensor width (6.2mm), and image dimension (4000x3000 pixels) parameters
188 of the Zenmuse X3 camera. Images were captured at a constant rate of 1 image every 2 seconds for both
189 cameras. A forward overlap of 90% at 100 meters translates to a flight speed of approximately 6.45 m/s and
190 a side overlap of 90% at 100 meters translates to transects approximately 17.2 meters apart. The RedEdge3
191 camera has a different focal length (5.4mm), sensor width (4.8mm), and image dimension (1280x960 pixels),
192 which translates to image overlap of 80.7/80.7 % at 100m below the lens and 83.9/83.9 % at ground level.
193 Approximately 1900 photos were captured over each 40 hectare survey area for each camera.

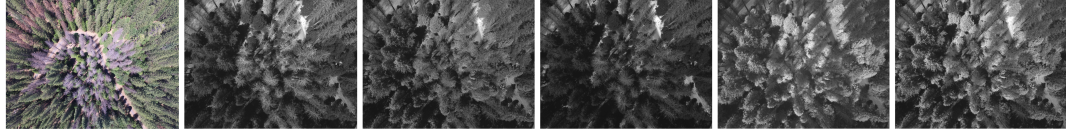
194 **Structure from Motion (SfM) processing**

195 We used structure from motion (SfM) to generate dense point clouds (Figure 3), digital surface models
196 (Figure 4), and orthorectified reflectance maps (Figure 5) for each field site (Frey et al. 2018). We used
197 Pix4Dmapper Cloud to process imagery using parameters ideal for images of a densely vegetated area taken
198 by a multispectral camera. For 29 sites, we processed the RedEdge3 multispectral imagery alone. For three
199 sites, we processed the RGB and the multispectral imagery in the same project to enhance the point density
200 of the resulting point cloud. All SfM projects resulted in a single processing “block,” indicating that all
201 images in the project were optimized and processed together.

202 **Creating canopy height models**

203 We classified each survey area’s dense point cloud into “ground” and “non-ground” points using a cloth
204 simulation filter algorithm (Zhang et al. 2016) implemented in the `lidR` (Roussel et al. 2019) package. We

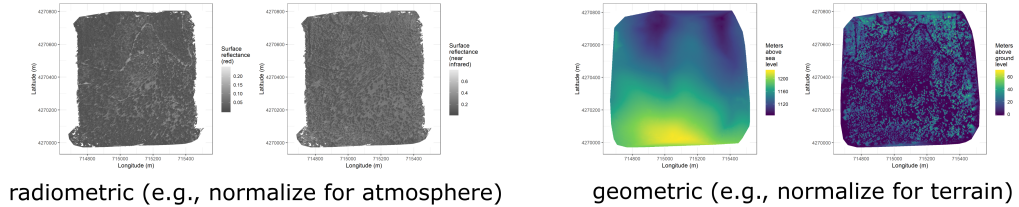
Level 0: raw data from sensors



Level 1: basic outputs from photogrammetric processing

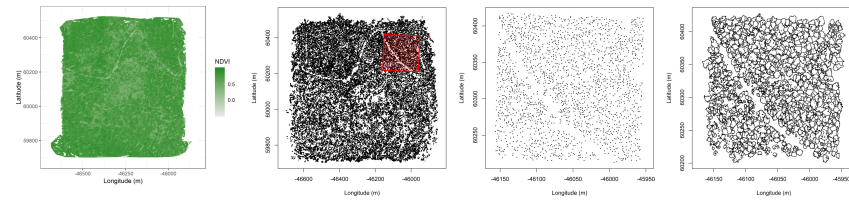


Level 2: corrected outputs from photogrammetric processing

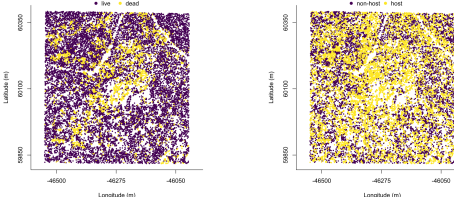


Level 3: domain-specific information extraction

L3a
spectral
OR
geometric



L3b
spectral
AND
geometric



Level 4: aggregations to regular grids

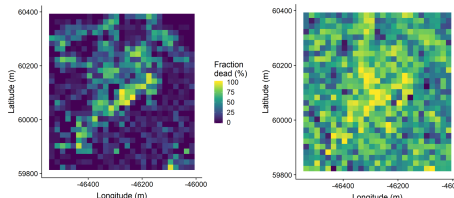


Figure 2: Schematic of the data processing workflow progressing from ‘Level 0’ raw data from the instruments to ‘Level 4’ aggregations of classified, geolocated trees to regular grid cells. Each data product is derived from lower data levels.

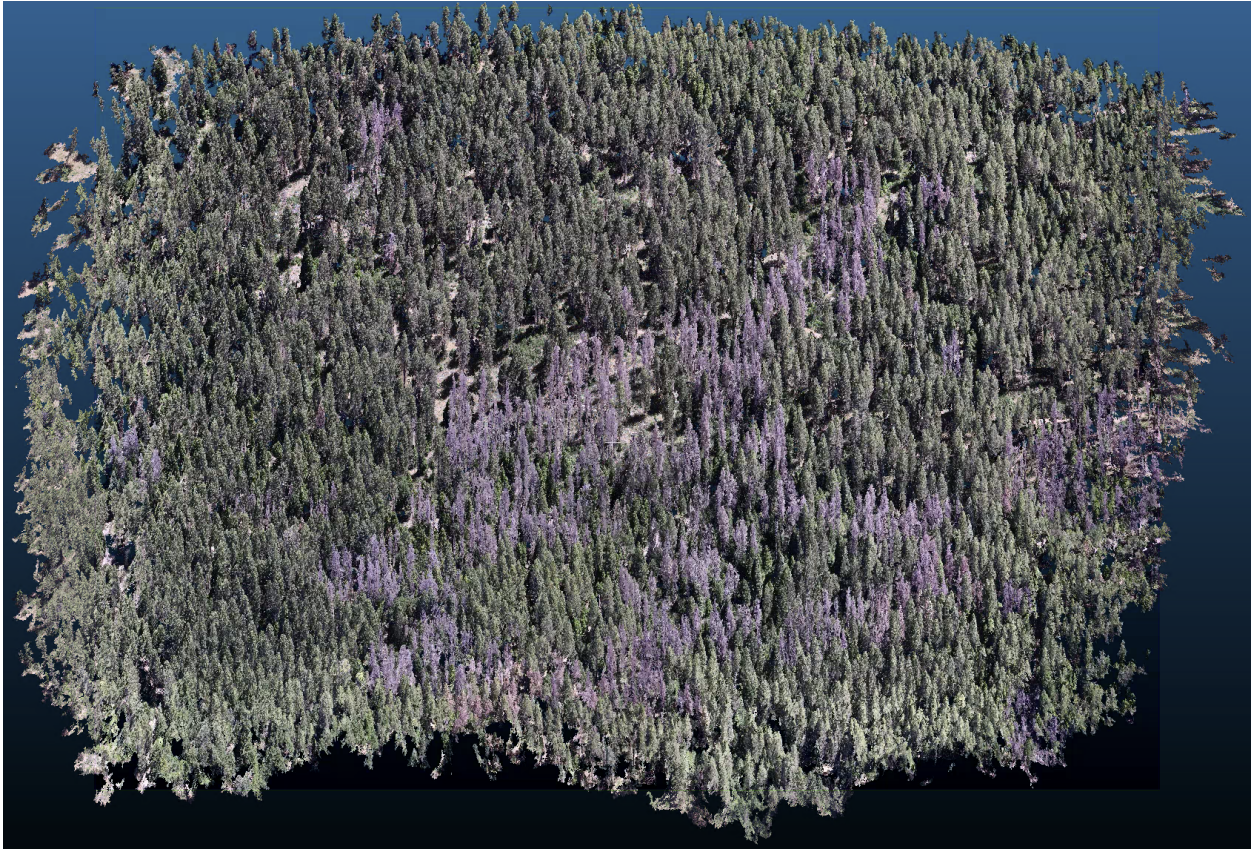


Figure 3: A dense point cloud representing ~40 hectares of forest is generated using Structure from Motion (SfM) processing of ~1900 images. The dense point cloud z- position represents the ground elevation plus the vegetation height.

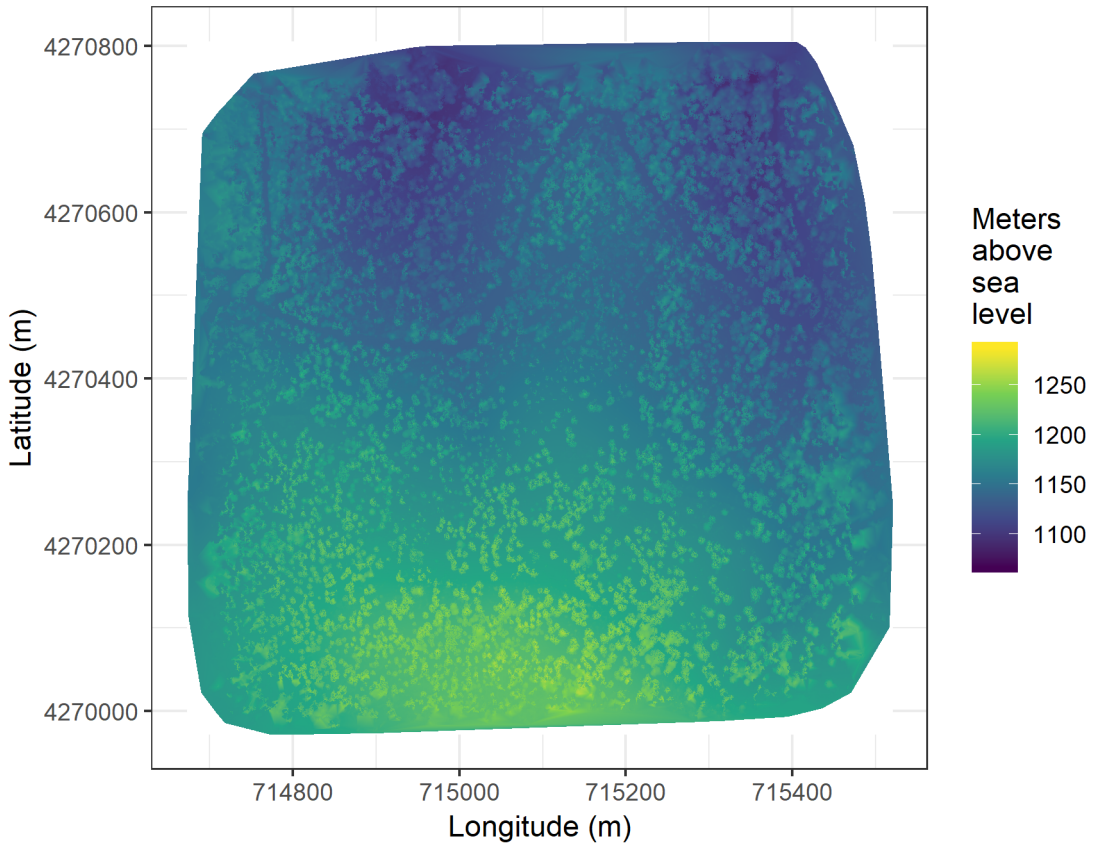


Figure 4: The digital surface model (DSM) is a 2-dimensional representation of the dense point cloud generated using structure from motion (SfM) processing. The DSM represents the ground elevation plus the vegetation height.



Figure 5: The orthomosaic for each of the 32 sites is generated with the Structure from Motion (SfM) processing, showing a top-down view of the whole survey area such that distances between objects in the scene are preserved and can be measured. Depicted is an example red-green-blue orthomosaic for one of the 32 sites covering approximately 40 hectares. The resolution of the original orthophoto is approximately 8cm per pixel, and has been considerably coarsened in this depiction.

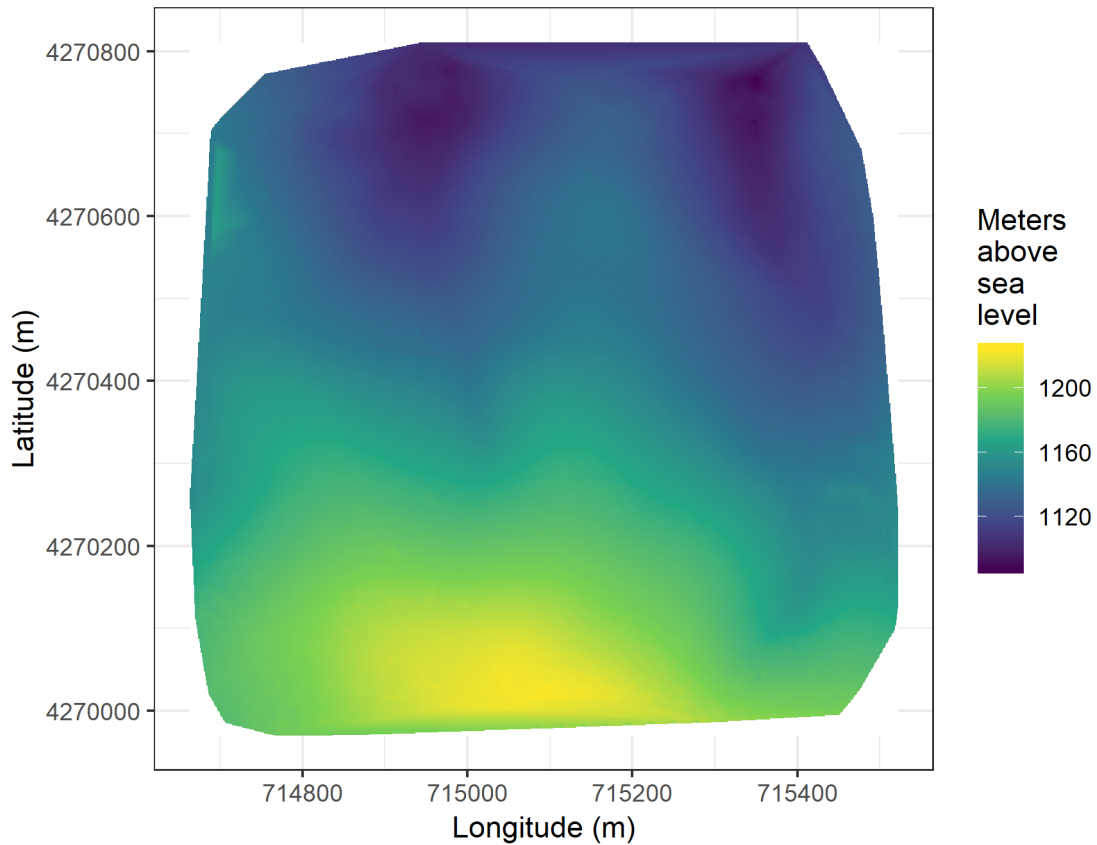


Figure 6: The digital terrain model (DTM) is generated by processing the dense point cloud using the cloth simulation filter algorithm (Zhang et al. 2016), which classifies points as ‘ground’ or ‘not-ground’ and then interpolates the ‘ground’ elevation using Delaunay triangulation for the rest of the dense point cloud footprint. The DTM represents the ground elevation without any vegetation.

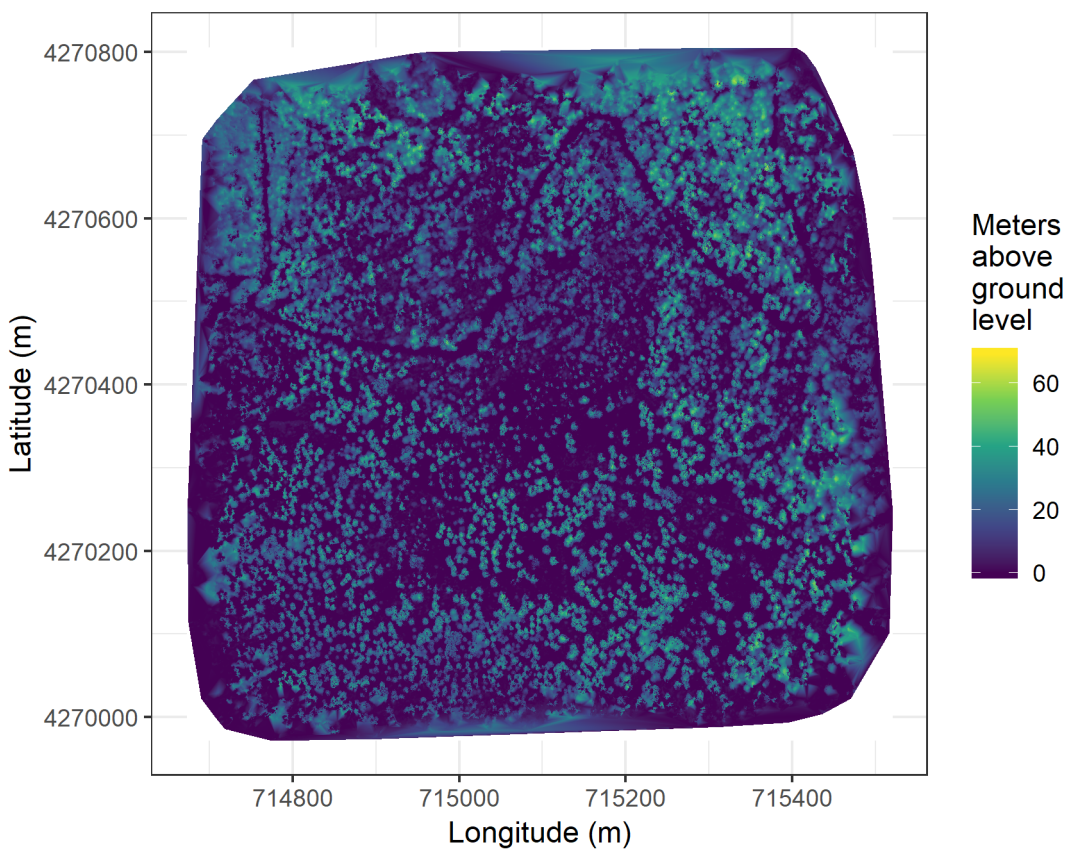


Figure 7: The canopy height model (CHM) is generated by subtracting the digital terrain model from the digital surface model. The CHM represents the height of all of the elevation above ground level.

205 rasterized the ground points using the `raster` package (Hijmans et al. 2019) to create a digital terrain model
 206 (Figure 6) representing the ground underneath the vegetation at 1 meter resolution. We created a canopy
 207 height model (Figure 7) by subtracting the digital terrain model from the digital surface model created in
 208 Pix4Dmapper.

209 **Tree detection**

210 We tested a total of 7 automatic tree detection algorithms and a total of 177 parameter sets on the canopy
 211 height model or the dense point cloud to locate trees within each site (Table 2). We used 3 parameter sets of
 212 a variable window filter using the `vwf()` function in the `ForestTools` (Plowright 2018) R package, including
 213 the default `winFun` parameter for the `vwf()` function as well as the “pines” and “combined” functions from
 214 Popescu and Wynne (2004) as the `winFun` parameter. We used 6 parameter sets of a local maximum filter
 215 implemented in `lidR`. We used 131 parameter sets of the algorithm from Li et al. (2012), which operates on
 216 the original point cloud. These parameter sets included those from Shin et al. (2018) and Jakubowski et
 217 al. (2013). We used 3 parameter sets of the `watershed` algorithm implemented in `lidR`, which is a wrapper
 218 for a function in the `EBImage` package (Pau et al. 2010). We used 3 parameter sets of `ptrees` (Vega et al.
 219 2014) implemented in `lidR` (Roussel et al. 2019) and `lidRplugins` (Roussel 2019) and which operates on
 220 the raw point cloud, without first normalizing it to height above ground level (i.e., subtracting the ground
 221 elevation from the dense point cloud). We used the default parameter set of the `multichm` (Eysn et al. 2015)
 222 algorithm implemented in `lidR` (Roussel et al. 2019) and `lidRplugins` (Roussel 2019). Finally, we used 30
 223 parameter sets of the experimental algorithm `lmfx` (Roussel 2019).

Table 2: Algorithm name, number of parameter sets tested for each algorithm, and references.

Algorithm	Parameter sets tested	Reference(s)
li2012	131	Li et al. (2012); Jakubowski et al. (2013); Shin et al. (2018)
lmfx	30	Roussel (2019)
localMaxima	6	Roussel et al. (2019)
multichm	1	Eysn et al. (2015)
ptrees	3	Vega et al. (2014)
vwf	3	Plowright (2018)
watershed	3	Pau et al. (2010)

224 Map ground data

225 Each orthorectified reflectance map was inspected to locate the 5 orange “X”s marking the center of the field
226 plots (Figure 5), though some plot centers were obscured due to dense interlocking tree crowns or because a
227 plot center was located directly under a single tree crown. We were able to locate 110 out of 180 field plots
228 and were then able to use these plots for validation of automated tree detection algorithms. We used the **sf**
229 package (Pebesma et al. 2019) to convert distance-from-center and azimuth measurements of each tree in the
230 ground plots to an x-y position on the SfM-derived reflectance map using the x-y position of the orange X
231 visible in the reflectance map as the center.

232 Correspondence of automatic tree detection with ground data

233 We calculated 7 forest structure metrics for each field plot using the ground data collected by Fettig et al.
234 (2019): total number of trees, number of trees greater than 15 meters, mean height of trees, 25th percentile
235 tree height, 75th percentile tree height, mean distance to nearest tree neighbor, mean distance to 2nd nearest
236 neighbor.

237 For each tree detection algorithm and parameter set described above, we calculated the same set of 7 structure
238 metrics within the footprint of the validation field plots. We calculated the Pearson’s correlation and root
239 mean square error (RMSE) between the ground data and the aerial data for each of the 7 structure metrics
240 for each of the 177 automatic tree detection algorithms/parameter sets.

241 For each algorithm and parameter set, we calculated its performance relative to other algorithms as whether
242 its Pearson’s correlation was within 5% of the highest Pearson’s correlation as well as whether its RMSE
243 was within 5% of the lowest RMSE. For each algorithm/parameter set, we summed the number of forest
244 structure metrics for which it reached these 5% thresholds. For automatically detecting trees across the whole
245 study, we selected the algorithm/parameter set that performed well across the most number of forest metrics
246 (Figure 8).

247 Segmentation of crowns

248 We delineated individual tree crowns with a marker controlled watershed segmentation algorithm (Meyer and
249 Beucher 1990) using the detected treetops as markers implemented in the **ForestTools** package (Plowright
250 2018). If the automatic segmentation algorithm failed to generate a crown segment for a detected tree (e.g.,
251 often snags with a very small crown footprint), a circular crown was generated with a radius of 0.5 meters. If
252 the segmentation generated multiple polygons for a single detected tree, only the polygon containing the
253 detected tree was retained (Figure 9). Image overlap decreases near the edges of the overall flight path, which

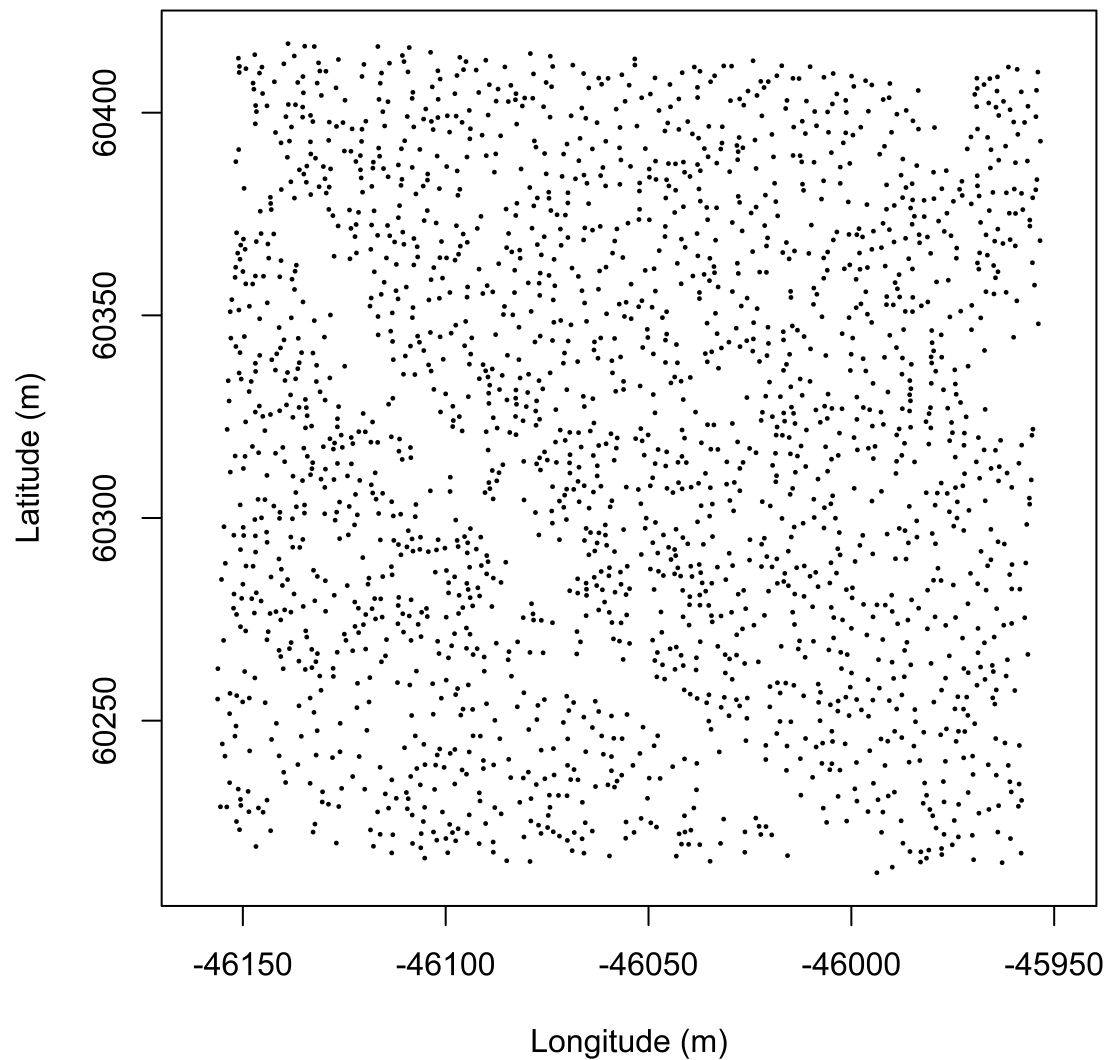


Figure 8: Tree locations are detected using the `lmfx` (Roussel et al. 2019) treetop detection algorithm on the dense point cloud.

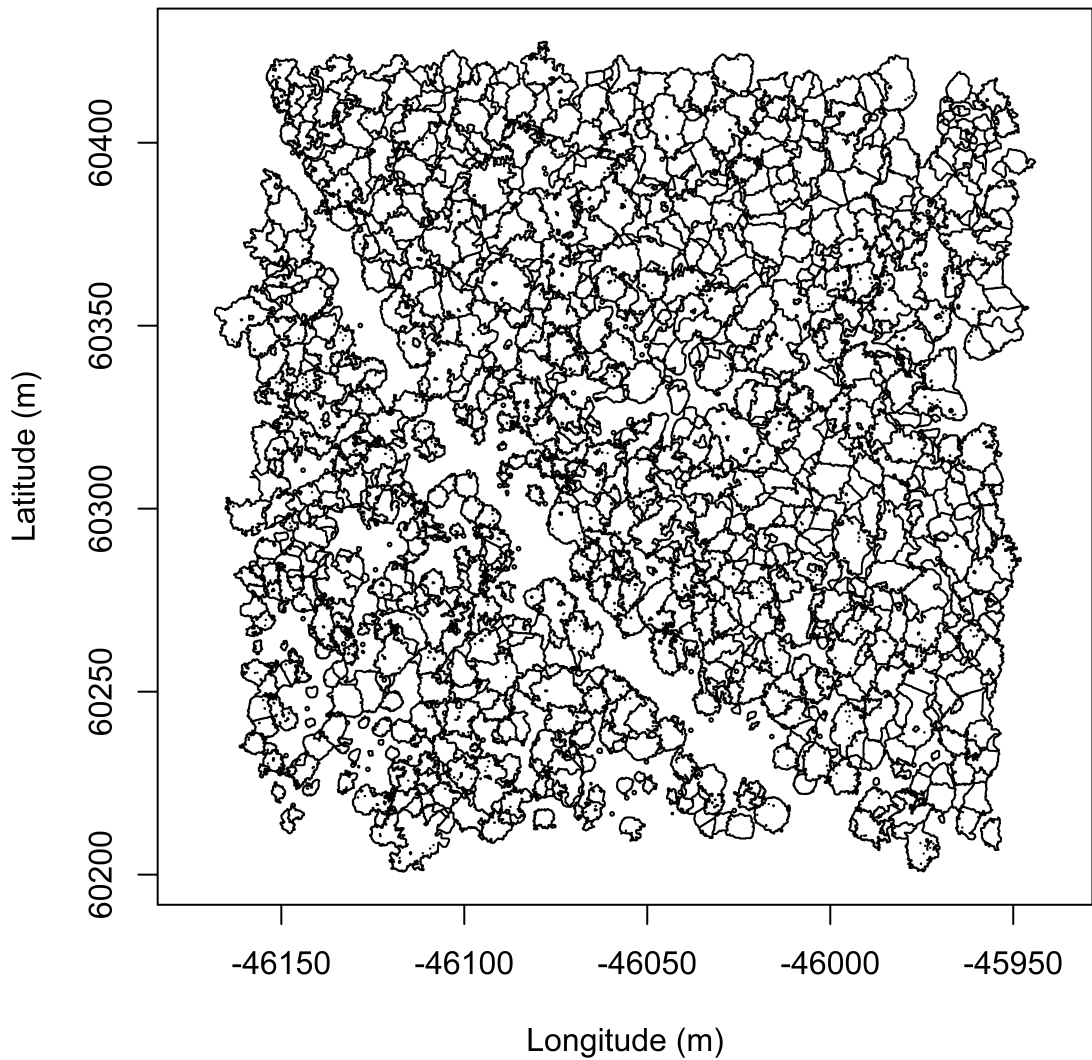


Figure 9: Individual crowns are delineated using a marker controlled watershed segmentation algorithm (Meyer and Beucher 1990, Plowright 2018) on the canopy height model (CHM) using the detected tree locations as a priority map. If the algorithm failed to delineate a crown for a tree that was identified in the tree detection step, a circular crown with a 0.5m buffer centered on point location of the detected tree was added as a crown.

reduces the quality of the SfM processing in those areas. Thus, we excluded segmented crowns within 35 meters of the edge of the survey area. Given the narrower field of view of the RedEdge3 multispectral camera versus the X3 RGB camera whose optical parameters were used to define the ~40 hectare survey area around each site, as well as the 35 meter additional buffering, the survey area at each site was approximately 30 hectares (Table 3).

We used the `velox` package (Hunziker 2017) to extract all the pixel values from the orthorectified reflectance map for each of the 5 narrow bands within each segmented crown polygon. Per pixel, we additionally calculated the normalized difference vegetation index (NDVI; Rouse et al. (1973)), the normalized difference red edge (NDRE; Gitelson and Merzlyak (1994)), the red-green index (RGI; Coops et al. (2006)), the red edge chlorophyll index ($CI_{red\ edge}$; Clevers and Gitelson (2013)), and the green chlorophyll index (CI_{green} ; Clevers and Gitelson (2013)). For each crown polygon, we calculated the mean value for each raw and derived reflectance band (5 raw; 5 derived).

Classification of trees

We overlaid the segmented crowns on the reflectance maps from 20 sites spanning the latitudinal and elevation gradient in the study. Using QGIS, we hand classified 564 trees as live/dead (Figure 10) and as one of 5 dominant species in the study area (*Pinus ponderosa*, *Pinus lambertiana*, *Abies concolor*, *Calocedrus decurrens*, or *Quercus kelloggii*) using the mapped ground data as a guide. We treated all trees classified as ponderosa pine as a “host” tree and all other species as “non-host” trees (Figure 11).

We used all 10 mean values of the reflectance bands for each tree crown polygon to predict whether the hand classified trees were alive or dead using a boosted logistic regression model implemented in the `caret` package (accuracy of live/dead classification on a withheld test dataset: 97.3%) (Kuhn 2008). For just the living trees, we similarly used all 10 reflectance values to predict the tree species using regularized discriminant analysis implemented in the `caret` package (accuracy of species classification on a withheld testing dataset: 66.7%; accuracy of WPB host/non-WPB-host (i.e., ponderosa pine versus other tree species) on a withheld testing dataset: 74.4%).

Finally, we used these models to classify all tree crowns in the data set as alive or dead as well as the species of living trees.

Allometric scaling of height to quadratic mean diameter

We converted the height of each tree determined using the canopy height model to its diameter at breast height, 1.37m (DBH). Using the tree height and DBH ground data from Fettig et al. (2019), we fit a simple

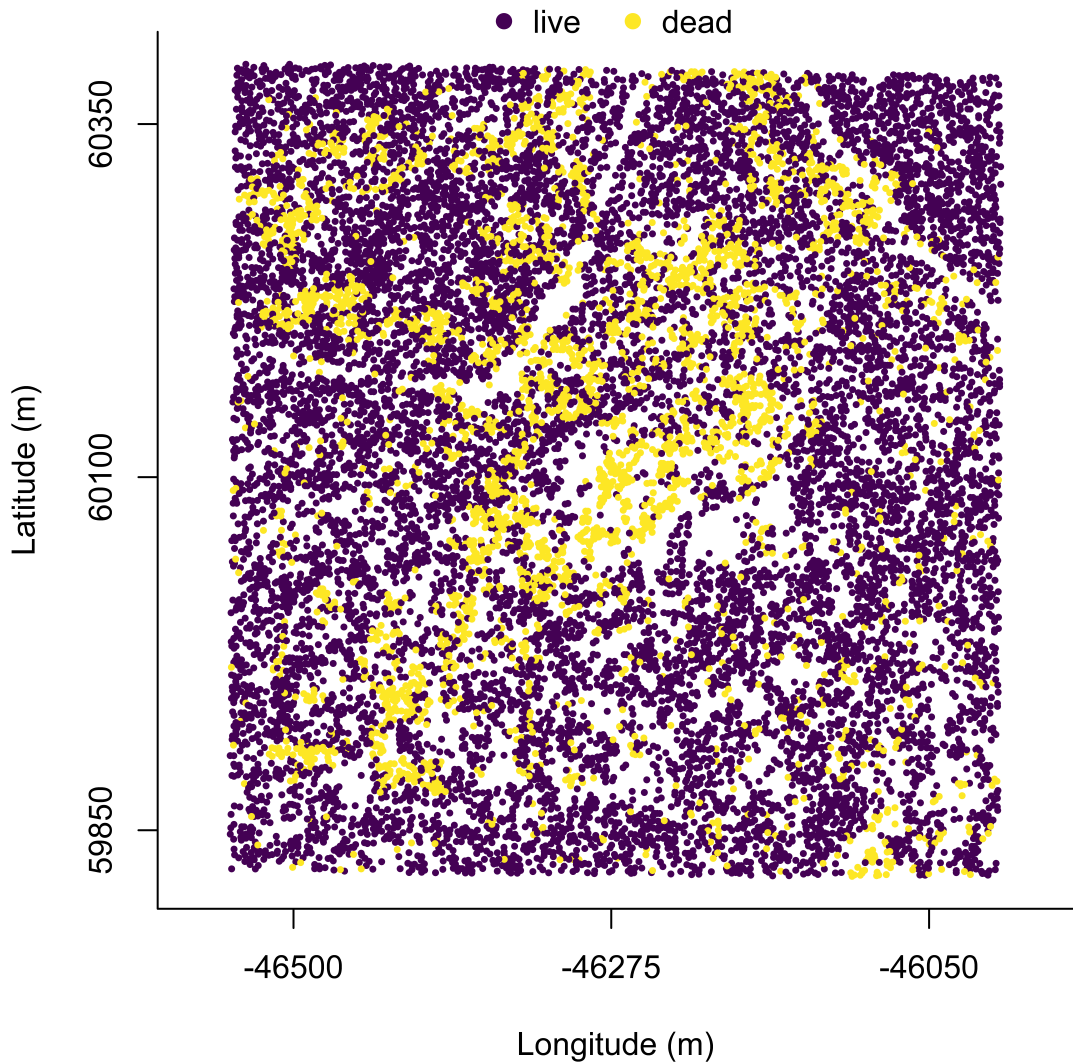


Figure 10: Each tree is classified as live or dead by extracting the pixel values from the 5 narrow bands of the Rededge3 camera (and 5 derived bands— see methods) in the orthomosaic within each segmented tree crown of the detected trees, taking their mean value, and using those means to predict live/dead status with a boosted logistic regression previously trained on a hand-classified set of segmented crowns from across the study area.

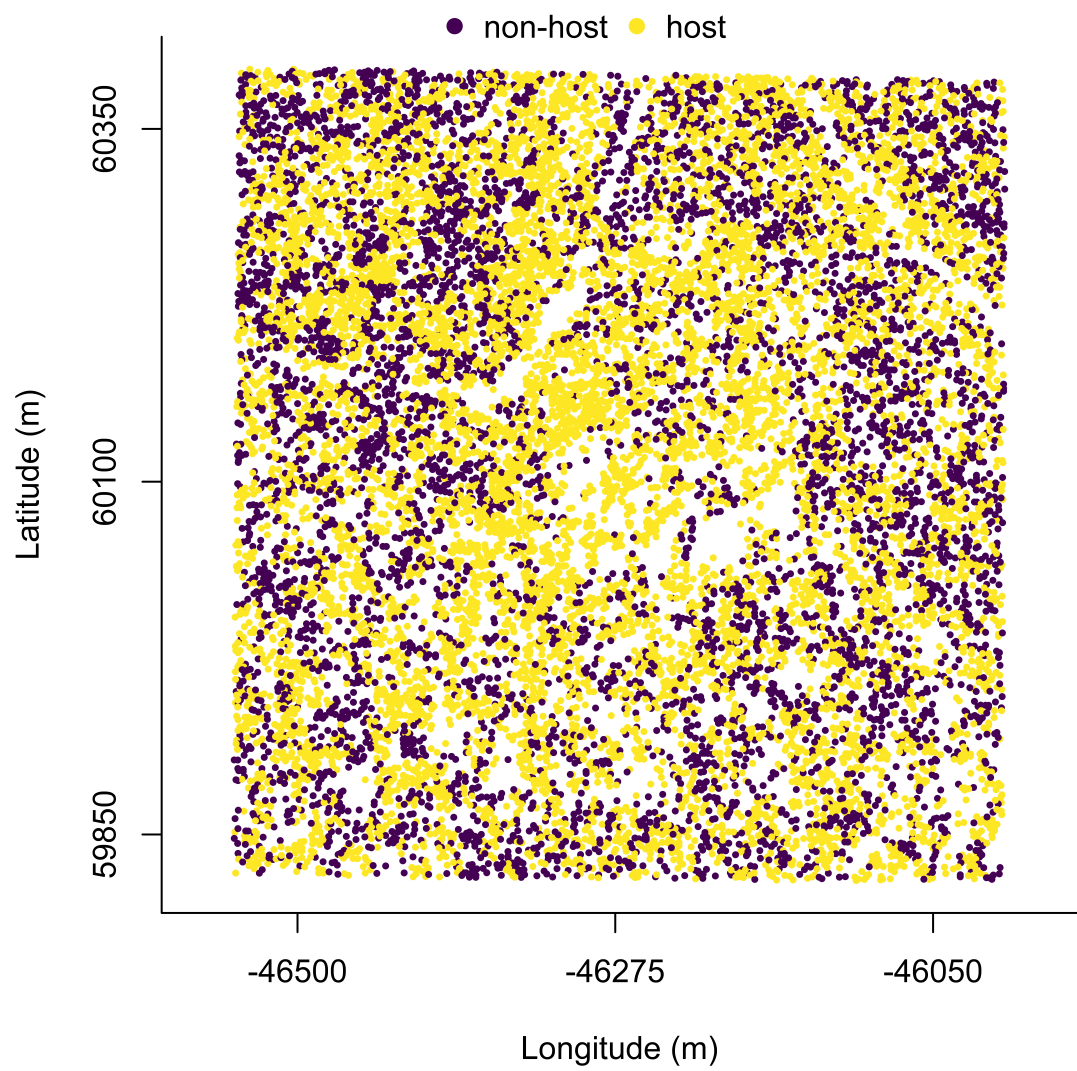


Figure 11: For each live tree, we classified its species using the same means of extracted pixel values across the 5 Rededge3 narrow bands (and 5 derived bands) as predictors in a regularized discriminant analysis previously trained on a hand-classified set of segmented crowns from across the study area.

284 linear regression to predict DBH from height for each of the 5 dominant species. Using the model-classified
285 tree species of each segmented tree, we used the corresponding linear relationship for that species to estimate
286 the DBH given the tree's height. We then calculated the quadratic mean diameter for each 20m x 20m cell as
287 the square root of the average squared diameter of trees within the cell.

288 **Note on assumptions about dead trees**

289 For the purposes of this study, we assumed that all dead trees were ponderosa pine and were thus host trees
290 for the western pine beetle. This is a reasonably good assumption for our study area, given that Fettig et al.
291 (2019) found that 73.4% of the dead trees in the coincident ground plots were ponderosa pine. The species
292 contributing to the next highest proportion of dead trees was incense cedar which represented 18.72% of the
293 dead trees in the ground plots. Incense cedar is not a potential host of the western pine beetle, and different
294 forest structure/environment conditions can dictate the dynamic between forest insects and their host tree
295 species (Stephenson et al. 2019). While the detected mortality is most likely to be ponderosa pine, it is
296 critical to interpret our results with this known limitation in mind.

297 **Rasterizing individual tree data**

298 Because the tree detection algorithms were validated against ground data at the plot level, we rasterized the
299 classified trees at a spatial resolution similar to that of the ground plots (Figure 12). That is, we rasterized
300 the individual tree data to 20m x 20m pixels equaling 400 m², and the circular ground plots with 11.35m
301 radius covered 404 m². In each raster cell, we calculated the: number of live trees, number of dead trees,
302 number of ponderosa pine trees, total number of trees (of all species, including ponderosa pine), quadratic
303 mean diameter (QMD) of ponderosa pine trees, and QMD of all trees of any species (overall QMD). We
304 converted the count of ponderosa pine trees and the total tree count to a density measurement of trees per
305 hectare (tpha) by multiplying the counts in each 20m x 20m cell by 25 to create a “host density” and an
306 “overall density” variable per cell.

307 **Environmental data**

308 We used climatic water deficit (CWD) (Stephenson 1998) from the 1981-2010 mean value of the basin
309 characterization model (Flint et al. 2013) as an integrated measure of temperature and moisture conditions
310 for each of the 32 sites. Higher values of CWD correspond to hotter, drier conditions and lower values
311 correspond to cooler, wetter conditions. CWD has been shown to correlate well with broad patterns of tree
312 mortality in the Sierra Nevada (Young et al. 2017) as well as bark beetle-induced tree mortality (Millar et al.
313 2012). We converted the CWD value for each site into a z-score representing that site's deviation from the

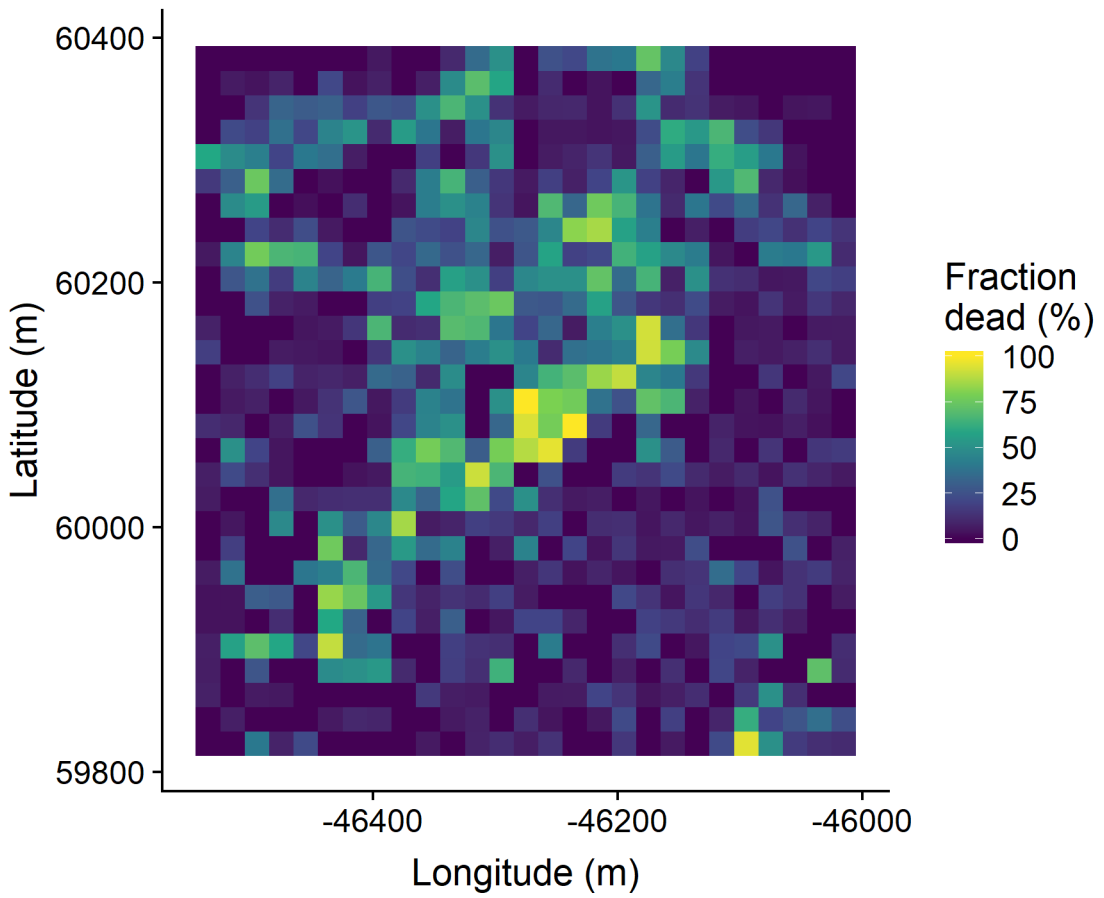


Figure 12: We rasterized the individual tree data by aggregating values to 20m x 20m cells. This example shows the proportion of dead trees per cell for the same example site as in the previous figures.

314 mean CWD across the climatic range of Sierra Nevada ponderosa pine as determined from 179 herbarium
 315 records described in Baldwin et al. (2017). Thus, a CWD z-score of one would indicate that the CWD at
 316 that site is one standard deviation hotter/drier than the mean CWD across all geolocated herbarium records
 317 for ponderosa pine in the Sierra Nevada.

318 **Statistical model**

319 We used a generalized linear model with a zero-inflated binomial response and a logit link to predict the
 320 probability of ponderosa pine mortality within each 20m x 20m cell as a function of the crossed effects of
 321 ponderosa pine quadratic mean diameter and density added to the crossed effect of quadratic mean diameter
 322 and density of trees of all species in each cell (hereafter “overall quadratic mean diameter” and “overall
 323 density”), as well as the interaction of each summand with climatic water deficit at each site.

324 To measure and account for spatial autocorrelation of the bark beetle behavioral processes underlying
 325 ponderosa pine mortality, we subsampled the data at each site to a random selection of 200, 20m x 20m cells
 326 representing approximately 27.5% of the surveyed area. With these subsampled data, we included a separate
 327 exact Gaussian process term per site of the interaction between the x- and y-position of each cell using the
 328 `gp()` function in the `brms` package (Bürkner 2017). The Gaussian process estimates the spatial covariance in
 329 the response variable (log-odds of ponderosa pine mortality) jointly with the effects of the other covariates.

$$y_{i,j} \sim \begin{cases} 0, & p \\ Binom(n_i, \pi_i), & 1 - p \end{cases}$$

$$\begin{aligned} logit(\pi_i) = & \beta_0 + \\ & \beta_1 X_{cwd,j} + \\ & \beta_1 X_{cwd,j} (\beta_2 X_{pipoQMD,i} + \beta_3 X_{pipoDensity,i} + \beta_4 X_{pipoQMD,i} X_{pipoDensity,i}) + \\ & \beta_1 X_{cwd,j} (\beta_5 X_{overallQMD,i} + \beta_6 X_{overallDensity,i} + \beta_7 X_{overallQMD,i} X_{overallDensity,i}) + \\ & \mathcal{GP}_j(x_i, y_i) \end{aligned}$$

330 Where y_i is the number of dead trees in cell i , n_i is the sum of the dead trees (assumed to be ponderosa pine)
 331 and live ponderosa pine trees in cell i , π_i is the probability of ponderosa pine tree mortality in cell i , p is the
 332 probability of there being zero dead trees in a cell arising as a result of an unmodeled process, $X_{cwd,j}$ is the
 333 z-score of climatic water deficit for site j , $X_{pipoQMD,i}$ is the scaled quadratic mean diameter of ponderosa
 334 pine in cell i , $X_{pipoDensity,i}$ is the scaled density of ponderosa pine trees in cell i , $X_{overallQMD,i}$ is the scaled

335 quadratic mean diameter of all trees in cell i , $X_{overallDensity,i}$ is the scaled density of all trees in cell i , x_i
 336 and y_i are the x- and y- coordinates of the centroid of the cell in an EPSG3310 coordinate reference system,
 337 and \mathcal{GP}_j represents the exact Gaussian process describing the spatial covariance between cells at site j .

338 We used 4 chains with 2000 iterations each (1000 warmup, 1000 samples), and confirmed chain convergence
 339 by ensuring all `Rhat` values were less than 1.1 (Brooks and Gelman 1998). We used posterior predictive
 340 checks to visually confirm model performance by overlaying the density curves of the predicted number of
 341 dead trees per cell over the observed number (Gabry et al. 2019). For the posterior predictive checks, we
 342 used 50 random samples from the model fit to generate 50 density curves and ensured curves were centered
 343 on the observed distribution, paying special attention to model performance at capturing counts of zero.

344 **Software and data availability**

345 All data are available via the Open Science Framework. Statistical analyses were performed using the `brms`
 346 packages. With the exception of the SfM software (Pix4Dmapper Cloud) and the GIS software QGIS, all
 347 data carpentry and analyses were performed using R (R Core Team 2018).

348 **Results**

Table 3: Site characteristics for each of the 32 sites. The site name consists of the forest name, elevation band, and rep separated by an underscore. The Eldorado National Forest is ‘elido’, the Stanislaus National Forest is ‘stan’, the Sierra National Forest is ‘sier’, and the Sequoia National Forest is ‘sequ’. The elevation band represents the lower bounds of the 305 meter (1000 foot) elevation bands in feet. Thus ‘3k’ implies that site was located between 3,000 and 4,000 feet (914-1219 meters). Aerially detected mortality and density of the whole site is presented along with the mortality and density calculated from the ground data (aerial / ground). The density is measured in trees per hectare (tpha).

Site	CWD (mm)	CWD (z-score)	Survey area (ha)	% tree mortality (aerial/ground)	Density (tpha; aerial/ground)
elido_3k_1	678	0.319	31.02	11/61	630/410
elido_3k_2	706	0.501	30.61	12/36	444/647
elido_3k_3	655	0.163	30.95	22/36	493/410
elido_4k_1	570	-0.383	28.04	9/39	633/588
elido_4k_2	642	0.0831	28.41	15/78	338/272
elido_5k_1	663	0.219	28.44	11/44	662/544
elido_5k_2	627	-0.0132	30.02	12/36	585/969
elido_5k_3	599	-0.2	29.73	7/32	489/623
stan_3k_1	638	0.059	31.04	10/52	739/1038

Site	CWD (mm)	CWD (z-score)	Survey area (ha)	% tree mortality (aerial/ground)	Density (tpha; aerial/ground)
stan_3k_2	739	0.713	18.78	40/78	434/405
stan_3k_3	762	0.859	30.1	22/41	558/326
stan_4k_1	540	-0.58	29.62	29/63	508/712
stan_4k_2	528	-0.658	30.54	18/56	482/257
stan_5k_1	524	-0.688	30.94	19/54	389/336
stan_5k_2	524	-0.685	29.94	21/44	399/623
sier_3k_1	764	0.871	30.42	19/48	651/850
sier_3k_2	768	0.898	30.05	20/77	439/153
sier_3k_3	773	0.932	29.77	32/77	511/460
sier_4k_1	841	1.38	30.43	54/51	576/539
sier_4k_2	764	0.877	29.3	33/57	499/855
sier_4k_3	688	0.383	26.39	48/59	454/499
sier_5k_1	722	0.599	14.59	41/43	631/717
sier_5k_2	710	0.523	27.53	53/74	477/455
sier_5k_3	779	0.968	28.93	33/43	569/484
sequ_4k_1	767	0.891	29.59	50/56	366/608
sequ_4k_3	816	1.21	29.69	35/71	433/306
sequ_5k_1	718	0.577	27.12	35/52	364/445
sequ_5k_2	587	-0.274	29.1	45/43	478/499
sequ_5k_3	611	-0.117	31.34	42/48	349/494
sequ_6k_1	731	0.657	27.78	30/70	433/361
sequ_6k_2	690	0.39	11.83	26/43	699/934
sequ_6k_3	603	-0.174	26.51	36/32	536/692

349 Tree detection

350 We found that the experimental `lmfx` algorithm with parameter values of `dist2d = 1` and `ws = 2.5` (Roussel
 351 et al. 2019) performed the best across 7 measures of forest structure as measured by Pearson's correlation
 352 with ground data (Table 4).

Table 4: Correlation and differences between the best performing tree detection algorithm (lmfx with dist2d = 1 and ws = 2.5) and the ground data. An asterisk next to the correlation or RMSE indicates that this value was within 5% of the value of the best-performing algorithm/parameter set. Ground mean represents the mean value of the forest metric across the 110 ground plots that were visible from the sUAS-derived imagery. The median error is calculated as the median of the differences between the air and ground values for the 110 visible plots. Thus, a positive number indicates an overestimate by the sUAS workflow and a negative number indicates an underestimate.

Forest structure metric	Ground mean	Correlation with ground	RMSE	Median error
total tree count	19	0.67*	8.68*	2
count of trees > 15m	9.9	0.43	7.38	0
distance to 1st neighbor (m)	2.8	0.55*	1.16*	0.26
distance to 2nd neighbor (m)	4.3	0.61*	1.70*	0.12
height (m); 25th percentile	12	0.16	8.46	-1.2
height (m); mean	18	0.29	7.81*	-2.3
height (m); 75th percentile	25	0.35	10.33*	-4

353 Effect of local structure and regional climate on western pine beetle severity

354 We detected a small, generally positive main effect of climatic water deficit on the probability of ponderosa
 355 pine mortality within each 20m x 20m cell (Figure 13).

356 We found a strongly positive main effect of ponderosa pine local density, with greater density increasing the
 357 probability of ponderosa pine mortality. Conversely, we found a strong negative effect of overall tree density
 358 (i.e., including both ponderosa pine and non-host species) such that additional non-host trees in a 20m x 20m
 359 cell (for the same number of host trees) would decrease the probability of ponderosa pine mortality (Figure
 360 13).

361 We found a generally negative effect of quadratic mean diameter of ponderosa pine on the probability of
 362 ponderosa mortality, suggesting that the western pine beetle attacked smaller trees, on average. There was a
 363 strong positive interaction between the climatic water deficit and ponderosa pine quadratic mean diameter,
 364 such that larger trees were more likely to increase the probability of ponderosa mortality in hotter, drier sites
 365 (Figure 14).

366 There was a positive interaction between overall tree density and overall quadratic mean diameter, such that
 367 denser stands with larger trees did lead to greater ponderosa pine mortality, though the main effects of each
 368 of these variables were weakly negative (Figure 13).

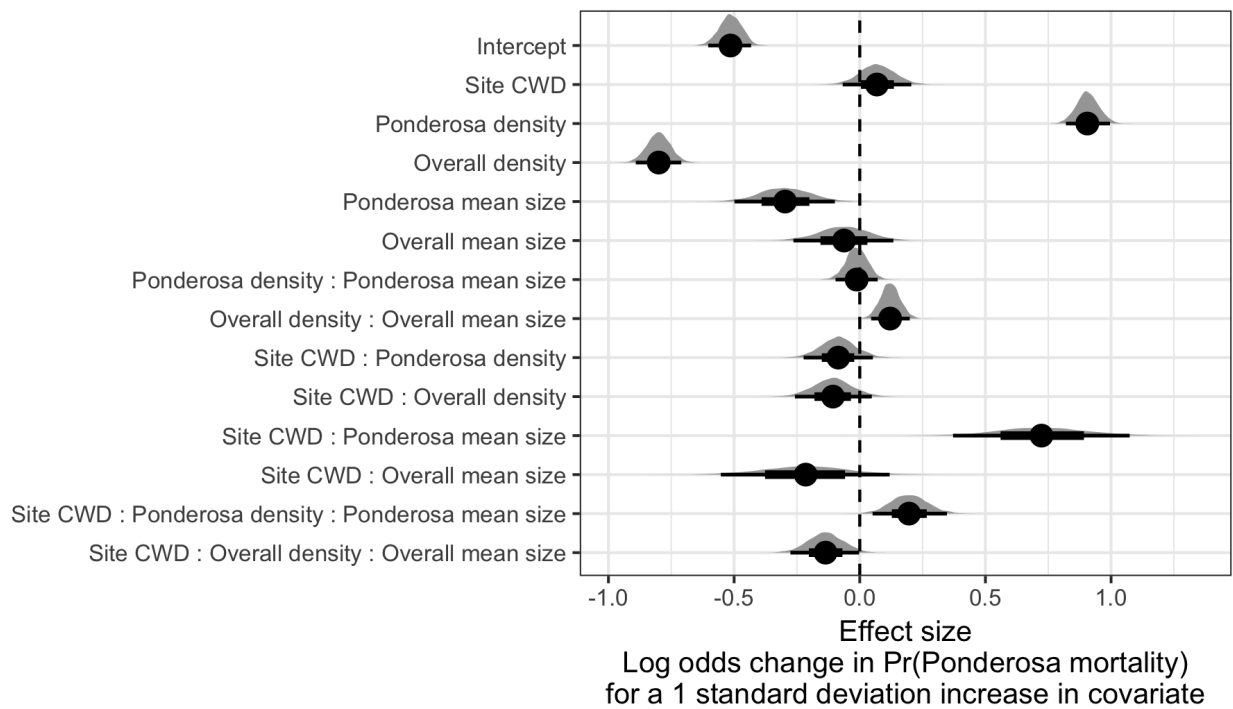


Figure 13: Posterior distributions of effect size from zero-inflated binomial model predicting the probability of ponderosa pine mortality in a 20m x 20m cell given forest structure characteristics of host trees and all trees within the cell, as well as a site-level climatic water deficit. The gray density distribution for each model covariate represents the density of the posterior distribution, the point underneath each density curve represents the median of the estimate, the bold interval surrounding the point estimate represents the 66% credible interval, and the thin interval surrounding the point estimate represents the 95% credible interval.

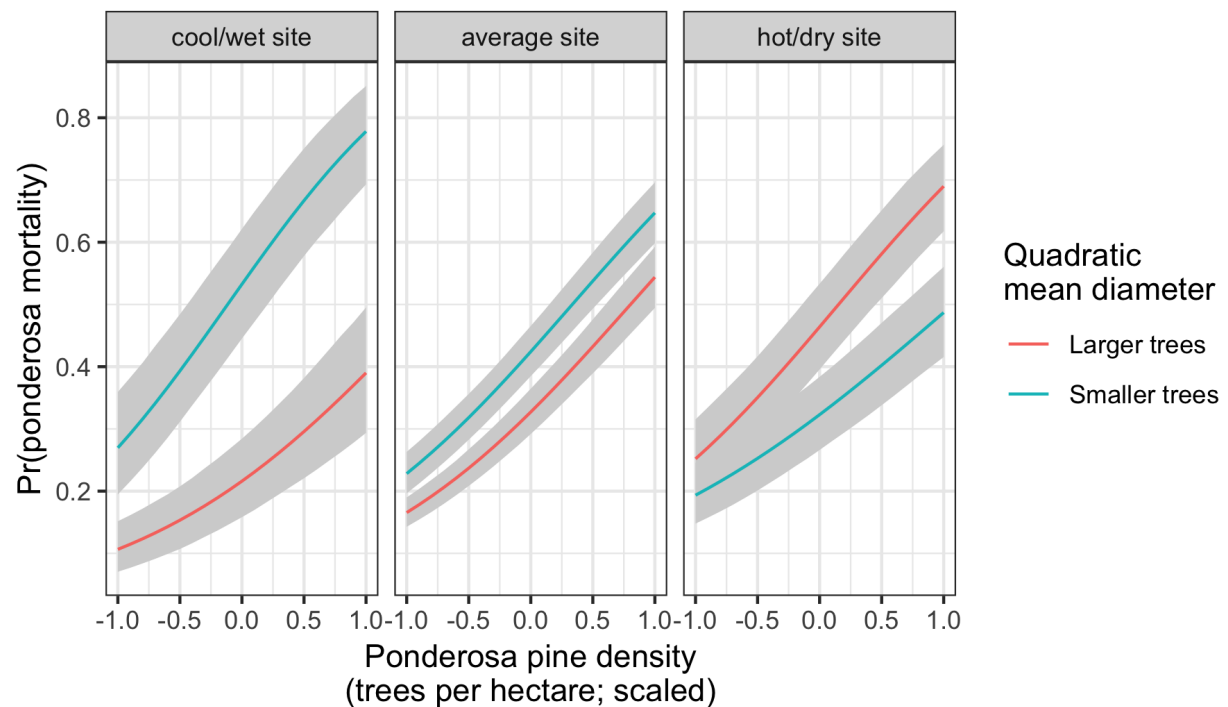


Figure 14: Line version of model results with 95% credible intervals showing primary influence of ponderosa pine structure on the probability of ponderosa pine mortality, and the interaction across climatic water deficit. The 'larger trees' line represents the quadratic mean diameter of ponderosa pine 0.7 standard deviations above the mean, and the 'smaller trees' line represents the quadratic mean diameter of ponderosa pine 0.7 standard deviations below the mean.

369 **Discussion**

370 We found that host tree density is a dominant driver of host mortality during elevated levels of bark beetle
371 activity, likely due to energy costs associated with beetles navigating forests with many non-hosts available.
372 We also found that, even within a single forest insect/tree species pairing, in the same extreme drought,
373 and conditional upon high levels of western pine beetle activity, host tree size may still strongly affect
374 insect-induced tree mortality in different ways depending on background environmental conditions of water
375 stress. We suggest that this may indicate different stages of bark beetle disturbance throughout the Sierra
376 yellow pine/mixed-conifer system, with “outbreak” thresholds surpassed at the hottest, driest sites where
377 larger trees led to more likely host mortality, but not yet surpassed in cooler, wetter sites, where smaller trees
378 led to more likely host mortality.

379 **Broad-scale environmental condition**

380 We were surprised to only find a weakly positive main effect of climatic water deficit on the probability of
381 ponderosa mortality, though an effect did materialize through its interaction with forest structure. We did
382 not measure tree water stress at an individual tree level as in other recent work (Stephenson et al. 2019), and
383 were instead treating climatic water deficit as a general indicator of tree stress following results of coarser-scale
384 studies (Asner et al. 2016, Young et al. 2017) which may have contributed to our failure to detect a strong
385 effect. Also, our entire study area experienced the same extreme hot drought between 2012 and 2015 and the
386 variation of mortality explained by a main effect of climatic water deficit may be dampened when most trees
387 are experiencing a high degree of water stress (Floyd et al. 2009, Fettig et al. 2019).

388 **Strength of support for different “density increases mortality” hypotheses**

389 The strongest effect on the probability of host mortality was the local host density within each 20m x 20m
390 cell. Host availability has been shown to have a strong influence on the prevalence of host mortality (Raffa
391 and Berryman 1987). This can arise as beetles require shorter flights to disperse to new hosts and beetles are
392 less likely to land on a non-host tree which imposes a “sunk cost” of energy expenditure in getting to that
393 tree. Reduced dispersal distances to host trees likely favors successful bark beetle attacks, but we calibrated
394 our aerial tree detection to ~400 m² areas rather than to individual tree locations so don’t have the data
395 precision to address this hypothesis directly. Because we also found a strong negative effect of overall tree
396 density (host plus non-host) within each cell while accounting for host density, we suspect that the positive
397 association between host density and host mortality might be driven by increasing the frequency that western
398 pine beetles land on their preferred host and avoid expending energy flying to non-hosts. The negative

399 relationship that we detected between overall tree density and host mortality corroborates findings from
400 Fettig et al. (2019) and perhaps the “sunk cost” of landing on non-hosts explains those findings, though
401 Fettig et al. (2019) didn’t simultaneously model the effect of host density. In general, Hayes et al. (2009)
402 and Fettig et al. (2019) found that measures of host availability explained less variation in mortality than
403 measures of overall tree density, but those conclusions were based on a response variable of “total number of
404 dead host trees,” rather than the number of dead host trees conditional on the total number of host trees as
405 in our study (i.e., a binomial response).

406 Counter to our expectations, we found an overall negative effect of host tree mean size on the probability of
407 host mortality. Generally, smaller trees are easier for western pine beetles to overwhelm in a mass attack and
408 are prime targets under normal levels of tree water stress. However, larger trees are more nutritious and
409 are therefore ideal targets if local bark beetle density is high enough to successfully initiate mass attack as
410 can occur when many trees are under severe water stress (Bentz et al. 2010). In the recent hot drought, we
411 expected that most trees would be under severe water stress, setting the stage for increasing beetle density,
412 successful mass attacks, and targeting of larger trees. Larger average tree size in this case would therefore
413 lead to greater ponderosa pine mortality, as was found in coincident ground plots (Fettig et al. 2019) and
414 other studies (Stephenson et al. 2019, Pile et al. 2019). One possible explanation for our finding is that our
415 observations represent the cumulative mortality of trees during a multi-year drought event and its aftermath.
416 Lower host tree mean size led to a greater probability of host mortality earlier in the drought (Pile et al.
417 2019) and that signal might have persisted even as mortality continued to accumulate driven by other factors.

418 We did find a clear host tree size effect in its interaction with the climatic water deficit. In hot, dry sites,
419 larger average host size increased the probability of host mortality while smaller host sizes increased the
420 probability of host mortality in cool, wet sites. This suggests that the same bark beetle species was cueing
421 into different aspects of forest structure across the environmental gradient. This represents an intraspecific
422 version of the results of Stephenson et al. (2019), who found that insect-induced tree mortality in the same
423 region during the same hot drought were driven by different factors for different tree species. For instance,
424 Stephenson et al. (2019) found that ponderosa pine mortality was largely driven by host selection behavior
425 of forest insects, where larger more nutritious trees were specifically targeted regardless of whether they
426 exhibited signs of stress. In contrast, Stephenson et al. (2019) found that white fir mortality occurred
427 predominantly in the slower growing, smaller, stressed trees. In our study, we found that, even within a single
428 pairing of forest insect species and its host, the host tree size affected host mortality differently depending on
429 the site-level climatic water deficit.

430 For aggressive bark beetles, massive tree mortality as observed from the 2012-2015 drought and its aftermath

431 does not necessarily distinguish “endemic” from “outbreak” phases of bark beetle disturbance, which is
432 instead distinguished by the underlying driver of bark beetle host selection behavior (Logan et al. 1998).
433 “Endemic” phases are distinguished by environmental determinism, when beetles select hosts based on whether
434 they are weakened in some way, often by environmental conditions. “Outbreak” phases are distinguished
435 by dynamic determinism, when population dynamics reign—when local beetle density is high enough that
436 intraspecific pheromone communication dominates host selection, successful mass attacks are likely, and even
437 large healthy trees can be killed (White and Powell 1997, Logan et al. 1998). Despite high local levels of
438 tree mortality across our study area (Fettig et al. 2019), our results from surveying the broader context
439 surrounding coincident ground plots reveals different effects of host tree size depending on the climatic water
440 deficit, and perhaps different stages of bark beetle disturbance across the environmental gradient. This may
441 help explain the especially high host mortality in high host density, low host size cells that we observed
442 in cool/wet sites (Figure 14). The smaller trees would presumably be nutritionally sub-optimal, and thus
443 unexpected targets if the western pine beetle were indeed in an “outbreak” phase at these sites and able to
444 attack even large, healthy trees. While trees were likely water stressed across the whole study due to the
445 extreme drought, we expected generally less water stress in the cool/wet sites, and generally higher water
446 stress in the hot/dry sites (Asner et al. 2016, Young et al. 2017). Thus, it is possible that the observed
447 mortality patterns across the Sierra Nevada during the 2012-2015 hot drought arose as synergistic alignment
448 of environmental conditions and complex forest structure enabled the western pine beetle to cross thresholds
449 of “outbreak” behavior in the hottest, driest sites but such an alignment was not present in the cooler, wetter
450 sites (Raffa et al. 2008).

451 Limitations and future directions

452 We have demonstrated that drones can be effective means of collecting data at multiple, vastly different
453 spatial scales to investigate a single, multi-scale phenomenon— from meters in between trees, to hundreds of
454 meters of elevation, to hundreds of thousands of meters of latitude. However, some limitations remain but
455 could perhaps be overcome with further refinements in the use of this tool for forest ecology. Most of these
456 limitations arise from tree detection and classification uncertainty, and thus it was imperative to work with
457 field data for calibration and uncertainty reporting.

458 The greatest limitation in our study arising from classification uncertainty is in the assumption that all dead
459 trees were ponderosa pine. We estimate from coincident ground plots that this is true approximately 73.4%
460 of the time. Because tree mortality response to forest insects is species-specific, even with sympatric tree
461 species during the same hot drought (Stephenson et al. 2019), we cannot entirely rule out that some of the

462 mortality responses to complex forest structure that we observed arose from these species-specific responses.
463 The overall community composition across our study area was not very different (Fettig et al. 2019), so we
464 remain confident that the patterns we observed were driven primarily by the dynamic between the western
465 pine beetle and ponderosa pine.

466 Our ability to detect trees using the geometry of the dense point clouds derived with the SfM was also
467 limited. The horizontal accuracy of the tree detection was better than the vertical accuracy, which may result
468 from a more significant error contribution by the ground-based calculations of tree height compared to tree
469 position relative to plot center (Table 4). Both the horizontal and vertical accuracy would likely improve
470 with better SfM point clouds, which requires imagery with more overlap. Frey et al. (2018) recently found
471 that 95% overlap was preferable for generating dense point clouds, and we only achieved 91.6% overlap with
472 the X3 RGB camera and 83.9% overlap with the multispectral camera. While our live/dead classification was
473 fairly accurate (97.3% on a withheld dataset), our species classifier would likely benefit from better crown
474 segmentation because the pixel-level reflectance values within each crown are averaged to characterize the
475 “spectral signature” of each tree. With better delineation of each tree crown, the mean value of pixels within
476 each tree crown will likely be more representative of that tree’s spectral signature. Better crown segmentation
477 would most readily be achieved through greater overlap in imagery. Finally, we anticipate that computer
478 vision and deep learning will prove helpful in overcoming some of these detection and classification challenges
479 (Gray et al. 2019).

480 Conclusions

481 Climate change adaptation strategies emphasize reducing tree densities to restore forest resilience (North et
482 al. 2015, Young et al. 2017), but understanding the optimal complex forest structure that can enable dry
483 western U.S. forests to persist through disturbances such as insect attack will be vital for predicting how
484 California forests may respond to these interventions. We’ve shown that drones can be a valuable tool for
485 investigating how this complexity in forest structure combines with environmental conditions to shape forest
486 insect disturbance.

487 Our results support conclusions of other researchers that management interventions to reduce the severity of
488 bark beetle disturbance will benefit from generally reducing tree density (Young et al. 2017). However, in
489 addition, our study suggests that outcomes will depend on whether the disturbance dynamic has crossed
490 endemic to outbreak feedback thresholds (Raffa et al. 2008), which may be predicted by recent advances in
491 disturbance forecasting (Preisler et al. 2017).

492 **Acknowledgements**

493 We gratefully acknowledge funding from the USDA Forest Service Western Wildlands Environmental Threat
494 Assessment Center (WWETAC) as well as Connie Millar for comments and guidance during the development
495 of this project.

496 **References**

- 497 Anderegg, W. R. L., J. A. Hicke, R. A. Fisher, C. D. Allen, J. Aukema, B. Bentz, S. Hood, J. W. Lichstein,
498 A. K. Macalady, N. McDowell, Y. Pan, K. Raffa, A. Sala, J. D. Shaw, N. L. Stephenson, C. Tague, and
499 M. Zeppel. 2015. Tree mortality from drought, insects, and their interactions in a changing climate. *New*
500 *Phytologist* 208:674–683.
- 501 Asner, G. P., P. G. Brodrick, C. B. Anderson, N. Vaughn, D. E. Knapp, and R. E. Martin. 2016. Progressive
502 forest canopy water loss during the 2012-2015 California drought. *Proceedings of the National Academy of*
503 *Sciences* 113:E249–E255.
- 504 Baldwin, B. G., A. H. Thornhill, W. A. Freyman, D. D. Ackerly, M. M. Kling, N. Morueta-Holme, and B. D.
505 Mishler. 2017. Species richness and endemism in the native flora of California. *American Journal of Botany*
506 104:487–501.
- 507 Bentz, B. J., J. Régnière, C. J. Fettig, E. M. Hansen, J. L. Hayes, J. A. Hicke, R. G. Kelsey, J. F. Negrón,
508 and S. J. Seybold. 2010. Climate change and bark beetles of the western United States and Canada: Direct
509 and indirect effects. *BioScience* 60:602–613.
- 510 Berryman, A. A. 1982. Population dynamics of bark beetles. Pages 264–314 in *Bark Beetles in North*
511 *American Conifers: A System for the Study of Evolutionary Biology*.
- 512 Brooks, S. P., and A. Gelman. 1998. General methods for monitoring convergence of iterative simulations.
513 *Journal of Computational and Graphical Statistics* 7:434.
- 514 Bürkner, P.-C. 2017. **brms**: An *R* package for bayesian multilevel models using *Stan*. *Journal of Statistical*
515 *Software* 80.
- 516 Chubaty, A. M., B. D. Roitberg, and C. Li. 2009. A dynamic host selection model for mountain pine beetle,
517 *Dendroctonus ponderosae* Hopkins. *Ecological Modelling* 220:1241–1250.
- 518 Clevers, J., and A. Gitelson. 2013. Remote estimation of crop and grass chlorophyll and nitrogen content using
519 red-edge bands on Sentinel-2 and -3. *International Journal of Applied Earth Observation and Geoinformation*
520 23:344–351.

- 521 Coops, N. C., M. Johnson, M. A. Wulder, and J. C. White. 2006. Assessment of QuickBird high spatial
522 resolution imagery to detect red attack damage due to mountain pine beetle infestation. *Remote Sensing of*
523 *Environment* 103:67–80.
- 524 DJI. 2015a. Zenmuse X3 - Creativity Unleashed. <https://www.dji.com/zenmuse-x3/info>.
- 525 DJI. 2015b. DJI - The World Leader in Camera Drones/Quadcopters for Aerial Photography. <https://www.dji.com/matrice100/info>.
- 527 DronesMadeEasy. 2018. Map Pilot for DJI on iOS. [https://itunes.apple.com/us/app/map-pilot-for-dji/
528 id1014765000?mt=8](https://itunes.apple.com/us/app/map-pilot-for-dji/id1014765000?mt=8).
- 529 Evenden, M. L., C. M. Whitehouse, and J. Sykes. 2014. Factors influencing flight capacity of the mountain
530 pine beetle (Coleoptera: Curculionidae: Scolytinae). *Environmental Entomology* 43:187–196.
- 531 Eysn, L., M. Hollaus, E. Lindberg, F. Berger, J.-M. Monnet, M. Dalponte, M. Kobal, M. Pellegrini, E.
532 Lingua, D. Mongus, and N. Pfeifer. 2015. A benchmark of LiDAR-based single tree detection methods using
533 heterogeneous forest data from the alpine space. *Forests* 6:1721–1747.
- 534 Farr, T. G., P. A. Rosen, E. Caro, R. Crippen, R. Duren, S. Hensley, M. Kobrick, M. Paller, E. Rodriguez, L.
535 Roth, D. Seal, S. Shaffer, J. Shimada, J. Umland, M. Werner, M. Oskin, D. Burbank, and D. Alsdorf. 2007.
536 The Shuttle Radar Topography Mission. *Reviews of Geophysics* 45.
- 537 Fettig, C. J. 2012. Chapter 2: Forest health and bark beetles. *in* Managing Sierra Nevada Forests. PSW-
538 GTR-237. USDA Forest Service.
- 539 Fettig, C. J. 2016. Native bark beetles and wood borers in Mediterranean forests of California. Pages 499–528
540 *in* Insects and diseases of Mediterranean Forest systems. Springer International Publishing, Switzerland.
- 541 Fettig, C. J., K. D. Klepzig, R. F. Billings, A. S. Munson, T. E. Nebeker, J. F. Negrón, and J. T. Nowak. 2007.
542 The effectiveness of vegetation management practices for prevention and control of bark beetle infestations in
543 coniferous forests of the western and southern United States. *Forest Ecology and Management* 238:24–53.
- 544 Fettig, C. J., L. A. Mortenson, B. M. Bulaon, and P. B. Foulk. 2019. Tree mortality following drought in the
545 central and southern Sierra Nevada, California, U.S. *Forest Ecology and Management* 432:164–178.
- 546 Flint, L. E., A. L. Flint, J. H. Thorne, and R. Boynton. 2013. Fine-scale hydrologic modeling for regional land-
547 scape applications: The California Basin Characterization Model development and performance. *Ecological*
548 *Processes* 2:25.
- 549 Floyd, M. L., M. Clifford, N. S. Cobb, D. Hanna, R. Delph, P. Ford, and D. Turner. 2009. Relationship of

- 550 stand characteristics to drought-induced mortality in three Southwestern piñonJuniper woodlands. Ecological
551 Applications 19:1223–1230.
- 552 Franceschi, V. R., P. Krokene, E. Christiansen, and T. Krekling. 2005. Anatomical and chemical defenses of
553 conifer bark against bark beetles and other pests. New Phytologist 167:353–376.
- 554 Frey, J., K. Kovach, S. Stemmler, and B. Koch. 2018. UAV photogrammetry of forests as a vulnerable
555 process. A sensitivity analysis for a structure from motion RGB-image pipeline. Remote Sensing 10:912.
- 556 Gabry, J., D. Simpson, A. Vehtari, M. Betancourt, and A. Gelman. 2019. Visualization in Bayesian workflow.
557 Journal of the Royal Statistical Society: Series A (Statistics in Society) 182:389–402.
- 558 Gitelson, A., and M. N. Merzlyak. 1994. Spectral reflectance changes associated with autumn senescence of
559 *Aesculus hippocastanum* L. And *Acer platanoides* L. Leaves. Spectral features and relation to chlorophyll
560 estimation. Journal of Plant Physiology 143:286–292.
- 561 Graf, M., M. Reid, B. Aukema, and B. Lindgren. 2012. Association of tree diameter with body size and lipid
562 content of mountain pine beetles. The Canadian Entomologist 144:467–477.
- 563 Gray, P. C., A. B. Fleishman, D. J. Klein, M. W. McKown, V. S. Bézy, K. J. Lohmann, and D. W. Johnston.
564 2019. A convolutional neural network for detecting sea turtles in drone imagery. Methods in Ecology and
565 Evolution 10:345–355.
- 566 Griffin, D., and K. J. Anchukaitis. 2014. How unusual is the 2012-2014 California drought? Geophysical
567 Research Letters 41:9017–9023.
- 568 Hayes, C. J., C. J. Fettig, and L. D. Merrill. 2009. Evaluation of multiple funnel traps and stand characteristics
569 for estimating western pine beetle-caused tree mortality. Journal of Economic Entomology 102:2170–2182.
- 570 Hijmans, R. J., J. van Etten, M. Sumner, J. Cheng, A. Bevan, R. Bivand, L. Busetto, M. Canty, D. Forrest,
571 A. Ghosh, D. Glicher, J. Gray, J. A. Greenberg, P. Hiemstra, I. for M. A. Geosciences, C. Karney, M.
572 Mattiuzzi, S. Mosher, J. Nowosad, E. Pebesma, O. P. Lamigueiro, E. B. Racine, B. Rowlingson, A. Shortridge,
573 B. Venables, and R. Wueest. 2019. Raster: Geographic data analysis and modeling.
- 574 Hunziker, P. 2017. Velox: Fast raster manipulation and extraction.
- 575 Jactel, H., and E. G. Brockerhoff. 2007. Tree diversity reduces herbivory by forest insects. Ecology Letters
576 10:835–848.
- 577 Jakubowski, M. K., W. Li, Q. Guo, and M. Kelly. 2013. Delineating individual trees from LiDAR data: A
578 comparison of vector- and raster-based segmentation approaches. Remote Sensing 5:4163–4186.

- 579 Kane, V. R., M. P. North, J. A. Lutz, D. J. Churchill, S. L. Roberts, D. F. Smith, R. J. McGaughey, J. T.
580 Kane, and M. L. Brooks. 2014. Assessing fire effects on forest spatial structure using a fusion of Landsat and
581 airborne LiDAR data in Yosemite National Park. *Remote Sensing of Environment* 151:89–101.
- 582 Kolb, T. E., C. J. Fettig, M. P. Ayres, B. J. Bentz, J. A. Hicke, R. Mathiasen, J. E. Stewart, and A. S. Weed.
583 2016. Observed and anticipated impacts of drought on forest insects and diseases in the United States. *Forest
584 Ecology and Management* 380:321–334.
- 585 Kuhn, M. 2008. Building predictive models in R using the caret package. *Journal of Statistical Software*
586 28:1–26.
- 587 Larson, A. J., and D. Churchill. 2012. Tree spatial patterns in fire-frequent forests of western North America,
588 including mechanisms of pattern formation and implications for designing fuel reduction and restoration
589 treatments. *Forest Ecology and Management* 267:74–92.
- 590 Li, W., Q. Guo, M. K. Jakubowski, and M. Kelly. 2012. A new method for segmenting individual trees from
591 the LiDAR point cloud. *Photogrammetric Engineering & Remote Sensing* 78:75–84.
- 592 Logan, J. A., P. White, B. J. Bentz, and J. A. Powell. 1998. Model analysis of spatial patterns in mountain
593 pine beetle outbreaks. *Theoretical Population Biology* 53:236–255.
- 594 Meyer, F., and S. Beucher. 1990. Morphological segmentation. *Journal of Visual Communication and Image
595 Representation* 1:21–46.
- 596 Micasense. 2015. MicaSense. <https://support.micasense.com/hc/en-us/articles/215261448-RedEdge-User-Manual-PDF-Download>
- 597 Millar, C. I., R. D. Westfall, D. L. Delany, M. J. Bokach, A. L. Flint, and L. E. Flint. 2012. Forest mortality in
598 high-elevation whitebark pine (*Pinus albicaulis*) forests of eastern California, USA: Influence of environmental
599 context, bark beetles, climatic water deficit, and warming. *Canadian Journal of Forest Research* 42:749–765.
- 600 Miller, J. M., and F. P. Keen. 1960. Biology and control of the western pine beetle: A summary of the first
601 fifty years of research. US Department of Agriculture.
- 602 Moeck, H. A., D. L. Wood, and K. Q. Lindahl. 1981. Host selection behavior of bark beetles (Coleoptera:
603 Scolytidae) attacking *Pinus ponderosa*, with special emphasis on the western pine beetle, *Dendroctonus
604 brevicomis*. *Journal of Chemical Ecology* 7:49–83.
- 605 Morris, J. L., S. Cottrell, C. J. Fettig, W. D. Hansen, R. L. Sherriff, V. A. Carter, J. L. Clear, J. Clement, R.
606 J. DeRose, J. A. Hicke, P. E. Higuera, K. M. Mattor, A. W. R. Seddon, H. T. Seppä, J. D. Stednick, and S.
607 J. Seybold. 2017. Managing bark beetle impacts on ecosystems and society: Priority questions to motivate

- 608 future research. *Journal of Applied Ecology* 54:750–760.
- 609 North, M. P., S. L. Stephens, B. M. Collins, J. K. Agee, G. Aplet, J. F. Franklin, and P. Z. Fule. 2015.
- 610 Reform forest fire management. *Science* 349:1280–1281.
- 611 Pau, G., F. Fuchs, O. Sklyar, M. Boutros, and W. Huber. 2010. EBImage: An R package for image processing
612 with applications to cellular phenotypes. *Bioinformatics* 26:979–981.
- 613 Pebesma, E., R. Bivand, E. Racine, M. Sumner, I. Cook, T. Keitt, R. Lovelace, H. Wickham, J. Ooms, K.
614 Müller, and T. L. Pedersen. 2019. Sf: Simple features for R.
- 615 Pile, L. S., M. D. Meyer, R. Rojas, O. Roe, and M. T. Smith. 2019. Drought impacts and compounding
616 mortality on forest trees in the southern Sierra Nevada. *Forests* 10:237.
- 617 Plowright, A. 2018. ForestTools: Analyzing remotely sensed forest data.
- 618 Popescu, S. C., and R. H. Wynne. 2004. Seeing the trees in the forest: Using LiDAR and multispectral data
619 fusion with local filtering and variable window size for estimating tree height. *Photogrammetric Engineering
620 and Remote Sensing*:16.
- 621 Preisler, H. K., N. E. Grulke, Z. Heath, and S. L. Smith. 2017. Analysis and out-year forecast of beetle,
622 borer, and drought-induced tree mortality in California. *Forest Ecology and Management*. 399: 166–178
623 399:166–178.
- 624 Raffa, K. F., B. H. Aukema, B. J. Bentz, A. L. Carroll, J. A. Hicke, M. G. Turner, and W. H. Romme. 2008.
625 Cross-scale drivers of natural disturbances prone to anthropogenic amplification: The dynamics of bark beetle
626 eruptions. *BioScience* 58:501–517.
- 627 Raffa, K. F., and A. A. Berryman. 1983. The role of host plant resistance in the colonization behavior and
628 ecology of bark beetles (Coleoptera: Scolytidae). *Ecological Monographs* 53:27–49.
- 629 Raffa, K. F., and A. A. Berryman. 1987. Interacting selective pressures in conifer-bark beetle systems: A
630 basis for reciprocal adaptations? *The American Naturalist* 129:234–262.
- 631 Raffa, K. F., J.-C. Grégoire, and B. Staffan Lindgren. 2015. Natural history and ecology of bark beetles.
632 Pages 1–40 in *Bark Beetles*. Elsevier.
- 633 R Core Team. 2018. R: A language and environment for statistical computing. R Foundation for Statistical
634 Computing, Vienna, Austria.
- 635 Rouse, W., R. H. Haas, W. Deering, and J. A. Schell. 1973. Monitoring the vernal advancement and
636 retrogradation (green wave effect) of natural vegetation. Type II Report, Goddard Space Flight Center,

- 637 Greenbelt, MD, USA.
- 638 Roussel, J.-R. 2019. lidRplugins: Extra functions and algorithms for lidR package.
- 639 Roussel, J.-R., D. Auty, F. De Boissieu, and A. S. Meador. 2019. lidR: Airborne LiDAR data manipulation
640 and visualization for forestry applications.
- 641 Seidl, R., J. Müller, T. Hothorn, C. Bässler, M. Heurich, and M. Kautz. 2016. Small beetle, large-scale
642 drivers: How regional and landscape factors affect outbreaks of the European spruce bark beetle. *The Journal
643 of applied ecology* 53:530–540.
- 644 Shiklomanov, A. N., B. A. Bradley, K. M. Dahlin, A. M. Fox, C. M. Gough, F. M. Hoffman, E. M. Middleton,
645 S. P. Serbin, L. Smallman, and W. K. Smith. 2019. Enhancing global change experiments through integration
646 of remote-sensing techniques. *Frontiers in Ecology and the Environment* 0.
- 647 Shin, P., T. Sankey, M. Moore, and A. Thode. 2018. Evaluating unmanned aerial vehicle images for estimating
648 forest canopy fuels in a ponderosa pine stand. *Remote Sensing* 10:1266.
- 649 Stephenson, N. 1998. Actual evapotranspiration and deficit: Biologically meaningful correlates of vegetation
650 distribution across spatial scales. *Journal of Biogeography* 25:855–870.
- 651 Stephenson, N. L., A. J. Das, N. J. Ampersee, and B. M. Bulaon. 2019. Which trees die during drought?
652 The key role of insect host-tree selection. *Journal of Ecology*:75.
- 653 Thistle, H. W., H. Peterson, G. Allwine, B. Lamb, T. Strand, E. H. Holsten, and P. J. Shea. 2004. Surrogate
654 pheromone plumes in three forest trunk spaces: Composite statistics and case studies. *Forest Science* 50.
- 655 USDAFS. 2019, February 11. Press Release: Survey finds 18 million trees died in California in 2018.
656 https://www.fs.usda.gov/Internet/FSE_DOCUMENTS/FSEPRD609321.pdf.
- 657 Vega, C., A. Hamrouni, S. El Mokhtari, J. Morel, J. Bock, J. P. Renaud, M. Bouvier, and S. Durrieu. 2014.
658 PTrees: A point-based approach to forest tree extraction from LiDAR data. *International Journal of Applied
659 Earth Observation and Geoinformation* 33:98–108.
- 660 White, P., and J. Powell. 1997. Phase transition from environmental to dynamic determinism in mountain
661 pine beetle attack. *Bulletin of Mathematical Biology* 59:609–643.
- 662 Young, D. J. N., J. T. Stevens, J. M. Earles, J. Moore, A. Ellis, A. L. Jirka, and A. M. Latimer. 2017.
663 Long-term climate and competition explain forest mortality patterns under extreme drought. *Ecology Letters
664* 20:78–86.

665 Zhang, W., J. Qi, P. Wan, H. Wang, D. Xie, X. Wang, and G. Yan. 2016. An easy-to-use airborne LiDAR
666 data filtering method based on cloth simulation. Remote Sensing 8:501.